Nonthermal Plasma Synthesis and Plasmonic Properties of Doped Silicon and Titanium Nitride Nanocrystals

A Thesis
SUBMITTED TO THE FACULTY OF THE
UNIVERSITY OF MINNESOTA
BY

Katelyn S. Schramke

IN PARTIAL FULFILLMENT OF THE REQUIREMENTS
FOR THE DEGREE OF
DOCTOR OF PHILOSOPHY

Prof. Uwe R. Kortshagen, Adviser

August 2017

Acknowledgements

The list of people I have to thank and acknowledge for their support and guidance throughout my graduate school career is long but I will try not to miss anyone. Thank you to my adviser, Uwe Kortshagen, for hiring me in the first place, keeping me around, and always pushing me forward. Thank you for always being supportive and offering your perspective when I needed it. I would like to acknowledge the other professors that helped me on my way through graduate school as well, especially Chris Hogan who was always willing to talk about research or football (Go Pack Go!), Eray Aydil who worked by my side to clean up pyrophoric liquid in the lab one day, Peter Bruggeman and Douglas Ernie for providing me with my formal plasma science education, and Sue Mantel for being someone I could go to for guidance from the very beginning (and giving me a bandage when I stubbed my toe on my way to our first meeting before I even started graduate school). I also want to give endless thanks the ME staff, many of which became friends over the years including, John Gardner (and of course our fellow Honey Badgers) who introduced me to curling and shared his wisdom, Karon Mooney for answering all of the questions all of the time, Jennifer Dahal, Jeanne, Julie, Gail, Richard, and of course Mike Leveille for all of his shop consultations and getting me to take the occasional lunch break. Thank you to Gary, Glen, Bob, Matt, and everyone else from the MNC for working with me on everything related to our nanocrystal system and the pleasant conversations when our workspaces overlapped. At this point, I should say that my friends, family, and research group members through the years have been so very important to me on this journey. It is hard to say if would have gotten this far without them but I know it was a much better path with them to help me carry the load along the way. Thank you to my fellow research group members for endless hours in the lab, conversations about ideas, and general support and motivation, it would be difficult to imagine a better group of people to work with: from the originals, Ben Greenberg – you and I started this journey at the same time and I couldn't have asked for a better lab mate and friend to go through this with, Jeslin Wu, Rebecca Anthony – you are my science role model, Nic Kramer, Dave Rowe, Ting Chen, Jason Trask, Andrew Wagner, and Jihua Yang – our long discussions about science and the English language were some of my favorites, to those that came and left during my time, Daryl Lee, Ranee Skinner – you can do anything you set your mind to and that is an inspiration, and Ben Pearce, to the ones stuck dealing with me while I finished up, Samantha Hill, Katharine Hunter, Kelsey Mork, Yunxiang Qin, Toshi Ono, Ali Eslamisaray, Zack Robinson, Jasmine Johnson, Chad Beaudette, and Sadhana Mishra. Extra thanks to Sam – my hunting buddy and seemingly the only person willing to give endless high/low fives, Katharine – my support and such a hardcore scientist, and Kelsey – my perspective, thank you for reminding me how important friendship is and how much better things can be when you have a great crew of women to tackle life's ups and downs with. Daryl and Jeslin, thank you for being the best office mates I could have asked for, the valuable insights, and the

adventures. Thank you to the other graduate students that I crossed paths with in classes or in the lab: Hallie Boyer – you stood by my side through the years, including the times we took quals, Srinidhi Murali, Grant Backes, Garrett Nelson, Zvie Razieli, Ivan Spector, Ben Adams – thanks for showing me that a small-town Wisconsin kid can make it, and Eric Victorson. I need to acknowledge Jes just a bit more. She has been by my side, my partner in crime in lab, the office, outside of work, and now on my google hangouts as a life adviser, she has been there every time I have needed it. Contrary to the long paragraph leading to this point, I have friends outside of the UMN as well who have encouraged and supported me for the last five years, admiring the science from a safe distance (some of you rooting for a lab accident that would lead to super powers) but always around to keep me heading in the right direction. Taylor "Spiffy" Murphy, John Riemer, and Tori Schoeneck have been lifelong friends, always there to motivate me and remind me of who I am, I love you guys. Paula, Chris, Tina and Patrick Geschwindner, Kelly and Kevin Lynch, Tom Bivens, thank you. Nick and Hitomi Iverson (along with Anna and Luka) for providing their home as a place to escape on weekends and letting me play with their kids and dogs and observe the American dream in real life. Joe Larson (and crew) for always being around to enjoy a beer, keeping me grounded, hosting the very best MNF venue there is, and being one of the truest friends. From my past life as a physicist, I need to thank Dr. B, Dr. McCann, and Dr. Madsen for pushing me as an undergraduate and helping to guide me along this path. Thank you to Michael Determan for introducing me to the world of industry research. Thank you all for coming along with me on the journey. Finally, I need to thank my family who have been there since the very beginning. Dana and Mary Beth Dawson, thank you for opening your home and doing what you could to make the last five years a little bit easier, for so many conversations, and for always being supportive. Dana, it was nowhere near the least you could have done. Thank you to the rest of the Dawson squad, Jef, Jan, John, and Debra (and cousins!) for being my home away from home and letting me know you're always there if I need you. Thank you to my brother and sister-in-law, Alex and Emily Schramke. Thank you to my wonderful grandma, Rachel Schramke, for believing in me, loving me no matter what, and for all the times you asked me how "that paper" is going. Kevin and Charlotte Schramke, my mom and dad. Thank you for your never-ending support, encouragement, and love. I could not have done it without you. Thank you all, for everything.

Dedication

This thesis is dedicated to Jihua Yang whose enthusiasm and presence are dearly missed.

Table of Contents

List of Tables

List of Figures

1. Introduction

1.1. Nonthermal Plasma Synthesis of Nanocrystals

Nanotechnology is currently a trending way of improving technology which is why nanomaterial related research has been of immense interest for the last couple decades. Some of the most common nanomaterial production techniques consist of liquid phase synthesis[1,2], thermal[3] and laser pyrolysis[4], and flame synthesis[5]. These processes, though having advantages for some materials and industries, also have their drawbacks, including use of hazardous solvents, particle agglomeration, and temperature restrictions. The nonthermal plasma process eliminates these issues and is a gas-phase, continuous production process. A nonthermal plasma has very energetic electrons that are at very high temperatures, around 50,000 K, and ions and neutrals that remain closer to room temperature. These nonequilibrium plasmas are partially ionized with an ionization fraction of 10^{-8} to 10^{-3} and have a plasma density of the order of $5x10^{10}$ cm^{-3}. In the synthesis process, precursor gases or aerosolized/vaporized liquids are flowed into the plasma region, where precursor atoms nucleate and grow into particles. The hot electrons interact energetically with the particles which heat them to temperatures significantly higher than the gas temperature which enables the process to successfully produce crystalline particles of materials with higher crystallization temperatures.[6] The particles are uniformly negatively charged which leads to Coulombic repulsion that eliminates particle agglomeration within the plasma.[7] The reactor walls are also

negatively charged which greatly reduces the amount of material lost during the process increasing the efficiency and extending equipment life. This nonthermal plasma synthesis technique has been used to generate silicon[7], doped silicon[8], germanium[9], gallium nitride[10], and zinc oxide[11] among other types of nanocrystals (NCs).

1.2. Localized Surface Plasmon Resonance

A localized surface plasmon resonance (LSPR) is the coupled oscillation of free carriers, electrons (n-type) or holes (p-type), that are dielectrically confined to a nanoparticle. The frequency of this oscillation facilitates the tunable absorbance that can be utilized for a wide variety of applications and is described in Equation 1, where f_{LSPR} is the plasmon frequency, N_{fc} the free carrier concentration, e is the electronic charge, ε_0 the free space permittivity, m_e the effective mass of the free carrier, ε_∞ the high frequency dielectric constant, and ε_m the dielectric constant of the surrounding medium.

Equation 1

$$f_{LspR} = \frac{1}{2\pi} \frac{N_{fc} e^2}{\left(\varepsilon_0 m_e^* (\varepsilon_\infty + 2\varepsilon_m)\right)^{1/2}}$$

The LSPR is dependent upon the free carrier concentration, nanoparticle size, shape, and dielectric surroundings. Plasmons couple strongly with incident light and generate large field enhancements as well as a significant absorption, which has been exploited in various applications including photocatalysis,[12,13] photodetection,[14,15] and increased efficiency of light-to-fuel devices.[16] Metal nanoparticles have a set number of free carriers that cannot be varied so LSPR can only be adjusted pre-synthesis by

modifying the size and shape of the nanoparticles and post-synthesis by changing the dielectric surroundings.[17–20] Active tunability of LSPRs over a broad spectral region is of interest in many relevant plasmonic applications. In order to achieve such a goal, different approaches have been followed, such as mechanical stretching of nanoparticle arrays on elastomeric substrates[21] or applied voltage controlled charge transfer plasmons.[22] Semiconductors can be doped to different carrier concentrations which gives an additional, very desirable, option for tuneability.[23–26] Plasmonically active metal nanoparticles tend to have resonances from the UV through the visible spectrum and are used for applications including spectroscopy enhancement[27,28] and biosensing[20,27,29]. Gold[30] and silver[31] nanomaterials are two of the most common plasmonic metals but other metals exhibit plasmonic behavior as well. Doped semiconductor nanoparticles with LSPRs have resonances from the near to mid infra-red and have potential applications in biosensing,[32,33] IR absorption spectroscopy enhancement,[34,35] and electrochromic light management[36] among others. Doped semiconductors that have been studied for their plasmon resonances include II-VI nanocrystals[17,37–40] like copper (I) sulfide,[40,41] phosphorus doped silicon,[42] aluminum doped zinc oxide,[43] transition-metal oxides,[44] and indium tin oxide.[45]

1.3. Thesis Overview

My research focused on the synthesis of doped silicon and titanium nitride (TiN) nanoparticles and the plasmonic behavior of the produced nanomaterials. I investigated

the effect of process controls on the properties of the resulting nanoparticles as well as the post-synthesis tuneability of the materials. Chapter 2 focuses on phosphorus doped (P-doped) and boron doped (B-doped) silicon nanocrystals (Si NCs) where the plasmonic behavior is used as way of understanding dopant behavior. It compares as-synthesized NCs to those that have undergone post-synthesis treatments and leads to a better understanding of dopant behavior in plasma synthesized Si NCs. Chapter 3 looks at controlling the morphology of P-doped Si NCs to make large, highly symmetric NCs. The effects of input power, electrode spacing, and precursor recipe on particle morphology are studied. Production of this type of NC would enable structural measurements of nanocrystalline P-doped silicon to be performed. Chapter 4 explores nonthermal plasma synthesis of TiN nanoparticles with plasmon resonance suitable for biological applications. This is the first instance, to the author's knowledge, at this time that a metalorganic precursor has been used with nonthermal plasma to produce TiN NCs. This recipe also yields a sharper, more stable LSPR than previously reported plasma synthesized TiN.

2. Plasmonic Properties of Silicon Nanocrystals Doped with Boron and Phosphorus

Parts of this chapter were adapted with permission from: Nicolaas J. Kramer; Katelyn S. Schramke; Uwe R. Kortshagen; Nano Lett. 2015, 15, 5597-5603. DOI: 10.1021/acs.nanolett.5b02287.

2.1. Abstract

Degenerately doped silicon nanocrystals are appealing plasmonic materials due to silicon's low cost and low toxicity. While surface plasmonic resonances of B-doped and P-doped silicon nanocrystals were recently observed, there is currently poor understanding of the effect of surface conditions on their plasmonic behavior. Here, we demonstrate that P-doped silicon nanocrystals exhibit a plasmon resonance immediately after their synthesis but may lose their plasmonic response with oxidation. In contrast, B-doped nanocrystals initially do not exhibit plasmonic response but become plasmonically active through post-synthesis oxidation or annealing. We interpret these results in terms of substitutional doping being the dominant doping mechanism for P-doped silicon nanocrystals, with oxidation-induced defects trapping free electrons. The behavior of B-doped silicon nanocrystals is more consistent with surface doping. Importantly, B-doped silicon nanocrystals exhibit air-stable plasmonic behavior over periods of more than a year.

2.2. Introduction

Nanocrystals (NCs) that exhibit a localized surface plasmon resonance (LSPR) have attracted attention for a wide range of applications from photothermal therapies,[46] to bioimaging and biosensing,[47,48] plasmonic enhancement of solar cells,[49] nanoelectronics,[50] hot electron generation for photocatalysis and photovoltaics,[51] and electrochromic materials.[52] These excitations provide a mechanism for enhancing and controlling many important processes such as energy transfer,[53,54] light-harvesting,[55,56] and hot carrier generation.[57,58] A variety of materials have been proposed for plasmonic applications spanning a wide range of wave- lengths.[59] In recent years degenerately doped semiconductor NCs have attracted significant attention. Contrary to noble metal NCs,[60] in which the carrier density is fixed, the position of the LSPR of doped semiconductor NCs can be tuned by adjusting the free carrier concentration of the NCs.[40]

Several strategies have been applied to control the free carrier concentration and the resulting LSPR of semiconductor NCs. The most common strategies are the extrinsic doping of semiconductors with n-type or p-type dopants,[42,61–63] the self-doping of compound semiconductors through the tuning of the NC composition,[64,65] and the doping through NC-solvent interactions.[66] Doping of semiconductor NCs allows for control over the LSPR wavelength while the NC size or shape remain unaffected. However, like many nanomaterials, doped semiconductor NCs suffer from oxidation and the strong influence of the NC surface conditions which may negatively impact their plasmonic properties. For instance, metal chalcogenides NCs, such as copper sulfide,

become increasingly doped during oxidation, resulting in an LSPR blue-shift.[67] Also, adsorbed surface species can trap free carriers such as in zinc oxide NCs where the plasmonic response may be completely eliminated through surface hydroxyl groups.[68]

There are opportunities for plasmonics to make an impact at longer wavelengths, particularly in the mid-IR.[69,70] Silicon NCs are potentially interesting nanomaterials for plasmonic applications in the infrared due to silicon's low cost and low toxicity. Recently, localized surface plasmon resonances were observed in highly P-doped and B-doped silicon nanocrystals (Si NCs) produced via nonthermal plasma synthesis.[42,63] However, the details of the influence of the NC surface on the dopant activation and plasmonic response are still poorly understood. Rowe *et al*. report tunable LSPRs of P-doped Si NCs right after the synthesis and kept under air-free conditions.[42] In contrast, Zhou *et al*. do not observe LSPRs of as-produced Si NCs, but report the occurrence of LSPRs only after long- time oxidation.[63] They suggest that long-time oxidation leads to a reduction of surface defect states that can trap free carriers and reduce the plasmonic response. In this paper, we study the evolution of the LSPRs of P-doped and B-doped Si NCs during oxidation and after post-synthesis annealing. Based on our results, we suggest that the plasmonic responses of P-doped and B-doped Si NCs is based on different mechanisms. The behavior observed for P-doped Si NCs appears consistent with substitutional doping and the subsequent trapping of free electrons at trap states at the silicon-silicon oxide interface. Contrarily, the LSPR of B-doped Si NCs is more

consistent with surface doping in which trap states play only a minor role. While substitutional boron is still present, it is insufficient by itself to reach the doping levels required for plasmonic behavior. Our work provides a better understanding of the effect of surface conditions and oxidation on the plasmonic response of Si NCs and suggest viable routes to achieve air-stable plasmonic Si NCs with controlled LSPRs in the infrared range of the spectrum.

2.3. Results and discussion

2.3.1. Plasmonic behavior of as-produced and oxidized NCs

Freestanding B-doped and P-doped Si NCs, with an average size of 8 nm, are produced using a nonthermal plasma process which has been described previously.[7,42,71] The indicated fractional dopant flow rates are defined as:

$$X_P = [PH_3]/([SiH_4]+[PH_3]) \times 100\% \quad \text{and}$$

$$X_B = 2[B_2H_6]/([SiH_4]+2[B_2H_6]) \times 100\%,$$

where $[P\ H_3]$, $[SiH_4]$ and $[B_2H_6]$ are the gaseous precursor flow rates of phosphine, silane, and diborane respectively. The Si NCs are deposited directly onto a glass substrate, silicon wafer or an aluminum-coated silicon wafer for further analysis. Fourier Transform Infrared Spectroscopy (FTIR) measurements of as-produced NCs are performed in a nitrogen-purged glovebox environment.

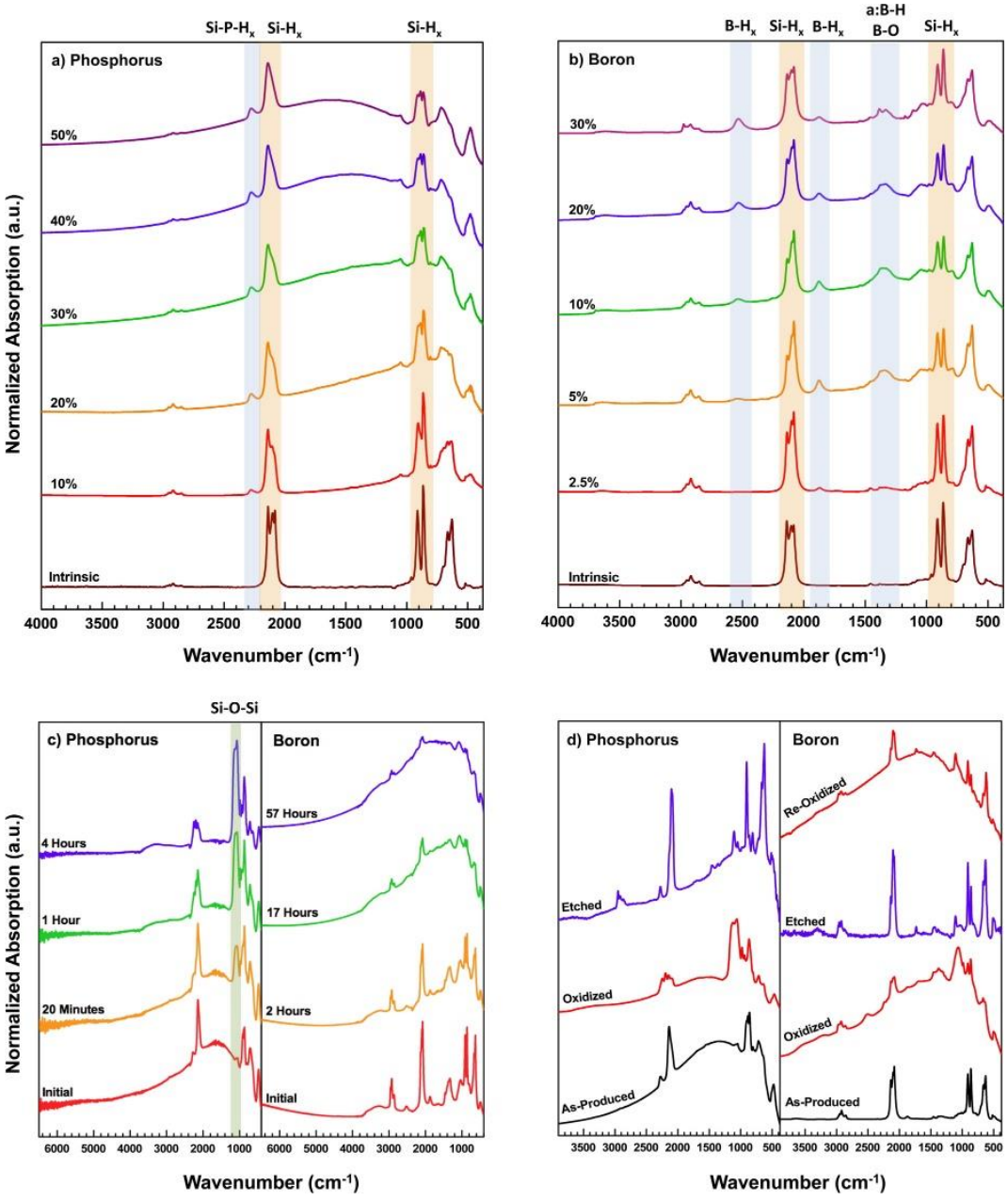

Figure 2.3.1 FTIR spectra of as-produced (a) P-doped and (b) B-doped silicon nanocrystals with increasing fractional doping flow rates. For P-doped Si NCs a LSPR emerges for sufficiently high doping concentrations. A LSPR is not visible for B-doped Si NCs, even at high doping levels. Absorption modes due to silicon-hydride, boron-hydride, and phosphorus-hydride related vibrations are observed, as indicated by the blue and orange regions. Spectra are offset for clarity. (c) Oxidation of P-doped (30%) and B-doped (2.5%) Si NCs in air as a function of time. Opposite behavior is observed, with the LSPR disappearing for P-doped Si NCs, while a LSPR develops and blue-shifts during oxidation for B-doped Si NCs. (d) Development of the LSPR for as-produced and subsequently oxidized and etched P-doped (30%) and B-doped (2.5%) Si NCs.

Figures 2.3.1a and 2.3.1b show the FTIR spectra of as-produced P-doped and B-doped Si NCs with increasing fractional dopant flow rates. These results illustrate a significant difference in plasmonic behavior between the two doping cases. For sufficiently high doping concentrations, a plasmon resonance emerges for P-doped Si NCs. The plasmon peak position blue-shifts for increasing fractional dopant flow rates as a result of the increased doping concentration. Using the peak position of the plasmon resonance,[40] we find a free carrier concentration of 1.9×10^{20} cm^{-3} for a fractional dopant flow rate of 30%. Assuming a nanoparticle size of 8 nm we estimate that highly P-doped Si NCs contain approximately 100 active phosphorus dopants per NC. In addition, there is a phosphorus-hydride stretch mode visible at 2276 cm^{-1} that becomes more pronounced for higher doping concentrations. This suggests that the surface of the NC also contains a significant amount of phosphorus which is likely inactive.[72,73] The as-produced NCs do not show any sign of oxidation as is confirmed by the absence of silicon oxide features in the spectra. Contrary to P-doped Si NCs, the as-produced B-doped Si NCs show no plasmon resonance, even at high fractional dopant flow rates. The boron-hydride and boron-oxide stretches at 2500 cm^{-1}, 1800 cm^{-1} and 1400 cm^{-1} indicate that boron is deposited on the surface of the Si NC during synthesis.[73,74] The lack of a plasmon resonance indicates a significantly smaller free carrier density compared to P-doped Si NCs. This difference in phosphorus and boron incorporation efficiency has been shown by various computational models,[75–77] in which the lower active boron concentration in Si NCs was attributed to

the larger formation energy of boron compared to phosphorus in Si NCs. Accordingly, the boron atoms prefer to reside on or near the surface of the Si NC where they do not affect the free carrier concentration.[78]

To investigate the role of the surface properties on the plasmonic properties we perform post-synthesis oxidation and annealing treatments. Figure 2.3.1c shows the effect of oxidation on P-doped and B-doped Si NCs as a function of oxidation time. Opposite behavior is again observed during oxidation. For the case of P-doped Si NCs, the LSPR vanishes as the NCs oxidize. A strong Si-O-Si bridging feature appears at 1050 cm^{-1} and a vibration related to silicon-hydride back-bonded oxygen (O_3-Si-H_X) around 2300 cm^{-1}. This suggests that oxidation of P-doped NCs reduces the number of free carriers, as the LSPR disappears after four hours of air exposure.

When B-doped Si NCs are exposed to oxygen, a LSPR emerges and blue-shifts as the particles oxidize. This suggests that oxidation induces the creation of additional free carriers. It is important to note that, different from P-doped Si NCs, no significant Si-O related absorption features are detected in the FTIR, even after 57 hours of oxidation. This indicates that the rate of oxidation is strongly reduced by the presence of boron at the Si NC surfaces. The oxidation-induced LSPR of B-doped silicon nanocrystals finally saturates after days of air exposure. After complete oxidation, the LSPR of B-doped silicon nanocrystals appears indefinitely stable and samples produced more than a year ago exhibit unchanged plasmonic response. This is an important observation for air-

stable plasmonic materials based in silicon nanocrystals.

The significant differences in oxidation rate of the P-doped and B-doped Si NCs is consistent with the Cabrera-Mott theory of oxidation of silicon.[79] According to this theory, electrons from the Fermi level of the Si NC core tunnel through the surface oxide to form negative ions of surface adsorbed oxygen. The process generates an electric field across the oxide which causes the oxygen ions to drift to the Si NC core. Phosphorus doping is expected to raise the Fermi level, which is consistent with the fast oxidation of the Si NCs due to the enhanced tunneling rate. Conversely, boron doping is expected to lower the Fermi level, which is supported by the significantly reduced oxidation rate of the B-doped Si NCs.

To further elucidate the effect of the surface oxidation, the oxide shell covering the Si NCs was removed using hydrofluoric acid (HF) vapor, followed by the measurement of FTIR spectra of etched, again oxide-free Si NCs. The FTIR spectra of the etched Si NCs are shown in Figure 2.3.1d. For P-doped Si NCs, the plasmon resonance returns after removal of the oxide but is red-shifted with respect to its original position. This suggests that some of the previously active phosphorus dopants are removed during etching, which is also confirmed by EDX measurements (see Figure 7.1.5 in Appendix, section 7.1). The complete removal of the oxide is confirmed by the lack of the two silicon oxide related absorptions around 1050 and 2300 cm^{-1} in the FTIR spectrum. Similar behavior was observed by Zhou *et al.*, where a strong plasmonic resonance appeared

after removal of the oxide.[63] For B-doped Si NCs the plasmon resonance disappears after etching and the new spectrum resembles that of the as-produced NCs. When the B-doped Si NCs re-oxidize, the plasmon resonance returns, confirming the need of an oxide shell for a plasmon resonance to develop. The peak position of the plasmon is not significantly affected by the etching and oxidation step, indicating that the free carrier density remains constant.

Previously it was suggested that a silicon oxide shell is required for plasmonic behavior, as it would provide a passivation route that reduces surface defect states.[63] Our findings do not support this hypothesis, since plasmonic behavior is only observed for oxidized boron- doped Si NCs. On the other hand, for P-doped Si NCs, the plasmonic properties deteriorate during oxidation. This suggests that the plasmonic response of silicon NCs is determined by oxidation-induced generation or removal of free carriers on the surface of the nanocrystal.

2.3.2. Surface defects and composition

Electron Paramagnetic Resonance (EPR) measurements were performed to gain insight into the number and type of defects at the surface of both types of doped Si NCs. Figure 2.3.2 shows the EPR spectra of intrinsic, B-doped and P-doped Si NCs. As-produced and oxidized spectra are shown in red and blue respectively. Two types of defects are visible for intrinsic Si NCs. A g-value of 2.0055 is assigned to threefold-

coordinated Si in a randomly distorted environment (D centers).[80] After oxidation the line shape and g-value change as a result of the formation of an oxide shell around the nanocrystals (P_b centers), which leads to trivalent silicon atoms at the interface of the silicon core and the oxide.[81]

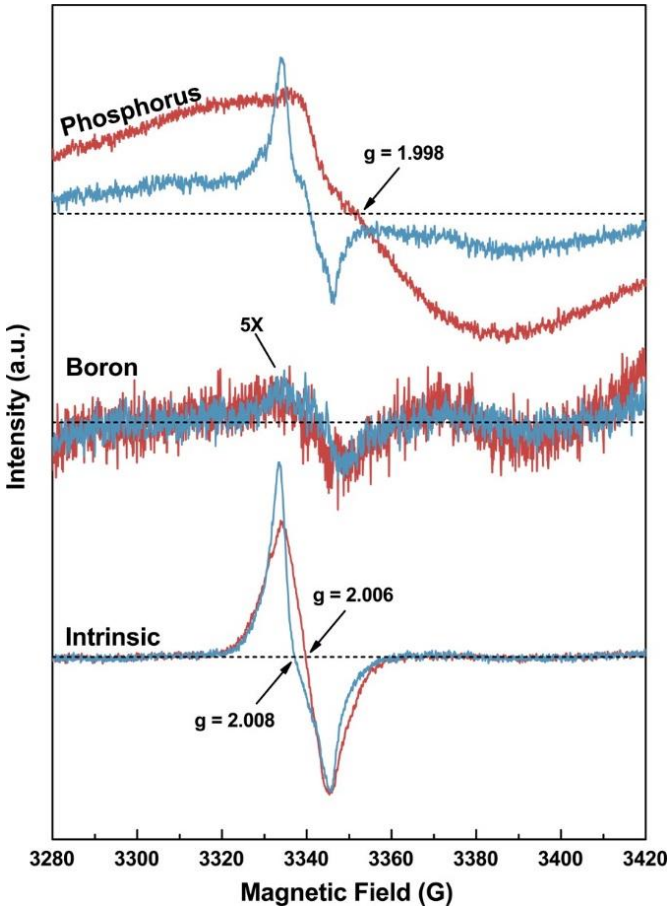

Figure 2.3.2 Electron paramagnetic resonance spectra for P-doped (10%), B-doped (10%), and intrinsic Si NCs. Spectra are shown for as-deposited (red) and oxidized (blue) NCs. The spectra for B-doped NCs have been magnified by a factor of 5 for clarity.

As-produced P-doped Si NCs exhibit a broad absorption with a g-value of 1.998. This is attributed to conduction electrons from active dopant atoms.[82–86] After oxidation the

magnitude of the broad feature reduces significantly and a traditional oxide signature appears, similar to oxidized intrinsic NCs. This confirms that oxidation is reducing the number of conduction electrons and indicates the generation of trap states while a silicon oxide shell is formed. This is consistent with the FTIR results, where the plasmonic response is lost during oxidation.

For B-doped Si NCs very little EPR signal is observed. The high concentration of boron atoms on the surface of the Si NC has been shown to lead to a passivation of the surface.[87] In contrast to P-doped Si NCs, oxidation of the B-doped Si NCs does not give rise to any further change of the spectrum. The lack of signal from P_b-centers, even after two weeks of oxygen exposure, implies that the B-doped Si NCs do not form a traditional silicon oxide shell. In particular, our results do not indicate a removal of dangling bonds at the surface due to oxidation as a source of the free carriers that cause the plasmonic response of oxidized B-doped Si NCs.

X-ray Photoelectron Spectroscopy (XPS) was used to further analyze the NC surface and dopant coordination. Figure 2.3.3 shows the XPS spectra of P-doped and B-doped NCs in as-produced and oxidized states. The P-doped Si NCs spectrum contains two features. The peak located at ~135 eV results from phosphorus bonded to oxygen. This peak is present for as-produced particles and is likely caused by the short air exposure during sample loading. A second peak at a lower binding energy of ~130 eV is a result of phosphorus bonded to phosphorus or silicon.[88] After oxidation the low

energy peak decreases in intensity compared to the higher energy oxide peak. This indicates that a significant fraction of phosphorus atoms that are bonded to silicon atoms and which may, at least in part, be active donors are oxidized and likely deactivated.

The boron XPS spectra in Figure 2.3.3 can be deconvolved into four peaks.[89–91] A broad peak at a low binding energy of ~185 eV is the contribution from the trivalent state of boron (B(III)). The feature at ~189 eV results from boron atoms bonded to four silicon or boron atoms. The two higher energy peaks originate from boron atoms that are attached to electronegative atoms such as oxygen. The XPS spectra indicate that a large fraction of trivalent boron is present, likely at the surface of the NC. Based on peak analysis, the fraction of trivalent boron of as-produced Si NCs is approximately 75%. After oxidation, this fraction does not decrease significantly. The spectrum of oxidized Si NCs shows a slight increase in intensity for the peaks corresponding to boron bonded to oxygen. This is consistent with the EPR results, which show almost no changes upon oxidation of the Si NCs. The significant importance of the surface conditions for the doping and plasmonic properties of Si NCs is apparent from the above observations. While in bulk semiconductors, substitutional placement of the dopants is essential, their properties at the NC surfaces clearly play a key role for the doping of Si NCs. The above observations of the difference in plasmonic behavior of P-doped and B-doped Si NCs suggest very different doping behavior for these two dopants. The presence of LSPRs in as-produced P-doped Si NCs seems to be consistent with an important role of

substitutional donors. The disappearance of the LSPR with oxidation of the Si NCs appears to be related to the generation of defect states at the silicon-silicon oxide interface. Substitutional doping in B-doped Si NCs seems to be less effective, as suggested by the lack of LSPR in as- produced Si NCs. Oxidation of B-doped Si NCs, where a large fraction of boron resides at the surface, leads to effective carrier generation, as evidenced by the appearance of the LSPR. The generation or removal of traps does not seem to play a significant role as suggested by the overall weak EPR signal and the complete lack of change of that signal during oxidation. While the carrier generation mechanism during the oxidation of B-doped Si NCs is currently not clear, it may be related to surface doping, as observed by Ristein.[92,93] In this mechanism, a surface dopant may accept an electron from the NC's valence band if its lowest unoccupied molecular orbital is close to the valance band maximum of the semiconductor NC, leading to the generation of free holes. It should be noted that some boron-oxide species have attachment energies that seem to be compatible with this process.[94]

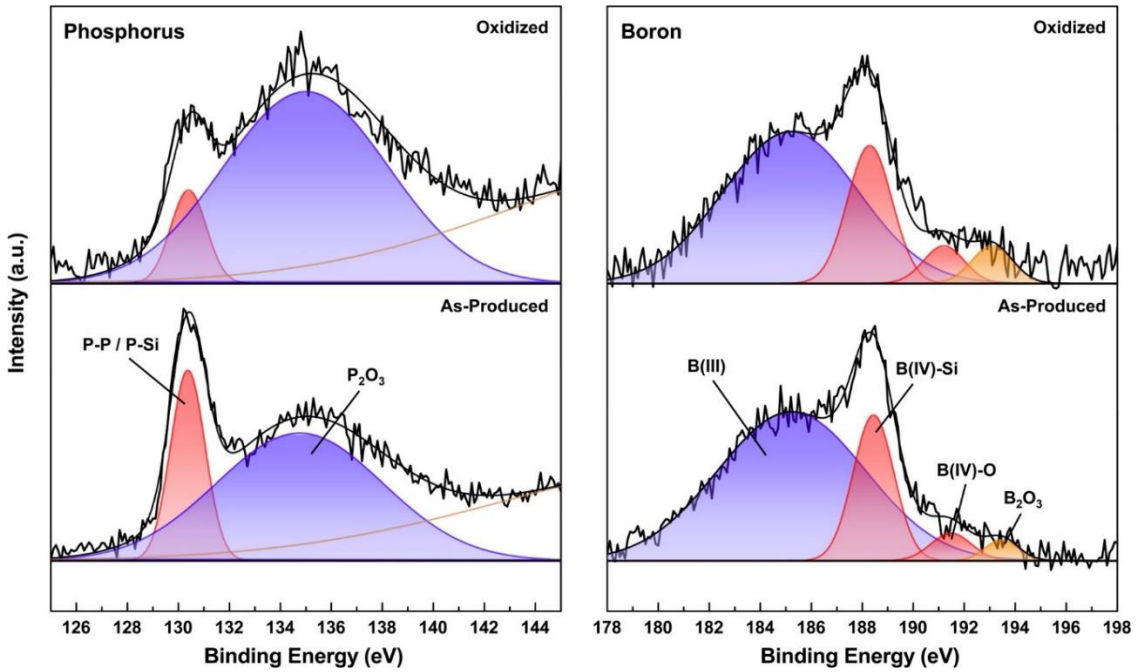

Figure 2.3.3 X-ray photoelectron spectroscopy (XPS) spectra for as-produced and oxidized P-doped (10%) and B-doped (10%) silicon NCs. The phosphorus spectrum can be deconvolved into two peaks. The peak at 130 eV corresponds to phosphorus bonded to phosphorus or silicon (red), while the broad peak at 135 eV is a result of oxidized phosphorus (blue). For boron, a broad peak at 185 eV originates from trivalent boron (blue) while the higher energy peak at 188 eV corresponds to tetravalent boron (red). The two peaks at 191 eV (red) and 193 eV (orange) are a result of oxygen bonding to boron.

2.3.3. Plasmonic behavior of annealed NCs

To further test this proposed mechanism, we studied the effect of low temperature annealing of Si NCs, which was found to reduce the defect density of Si NCs by more than an order of magnitude.[80] The FTIR spectra of P-doped and B-doped Si NCs annealed at low temperature in a nitrogen environment is shown in Figure 2.3.4a. The Si NCs were annealed on a hotplate in an oxygen-free glovebox environment with less than 0.1 ppm of oxygen for ten minutes at each specified temperature and the FTIR

spectrum was measured after the samples cooled down to room temperature. P-doped Si NCs exhibit a blue-shift of the LSPR which may indicate an increase in the free electron density due to the removal of trap states, as confirmed by EPR measurements (see Figure 7.1.6 in Appendix, section 7.1). Annealing also leads to the appearance of LSPRs for the annealed B-doped Si NCs. This may be an effect of accelerated oxidation of the B-doped Si NCs at higher temperatures, as small Si-O-Si features become visible at 1050 cm^{-1} likely due to reaction with trace oxygen in the glovebox. Additionally, restructuring of the surface may be contributing to the induced plasmon resonance during annealing.

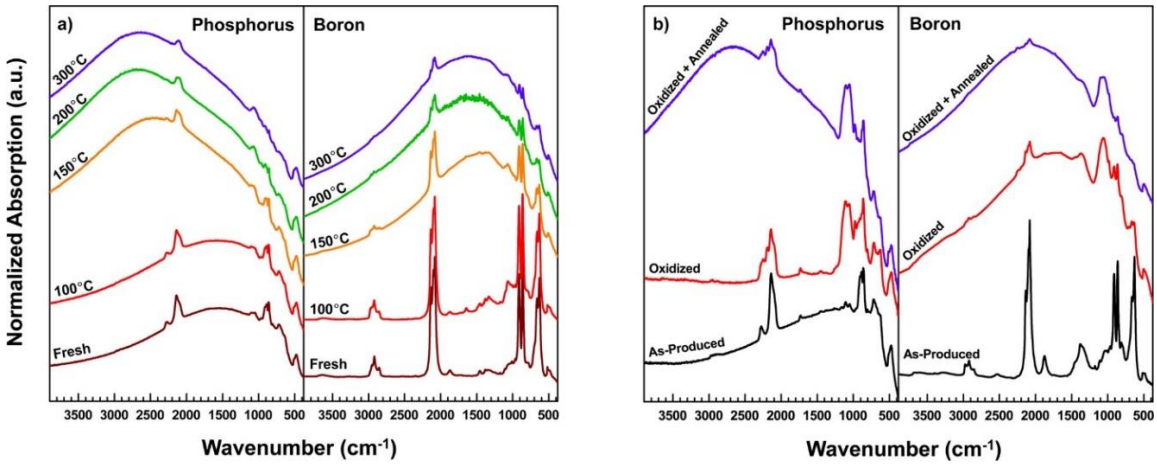

Figure 2.3.4 (a) Development of the LSPR during low-temperature air-free annealing of phosphorus (30%) and B-doped (2.5%) Si NCs. As a result of the annealing step the LSPR significantly blue-shifts for P-doped Si NCs. For B-doped Si NCs, the annealing treatment is able to generate additional free carriers, leading to a plasmon resonance to develop. (b) FTIR spectra of as-produced, oxidized and subsequent annealed at 200 °C P-doped and B-doped silicon NCs. While the LSPR is removed after oxidation, an annealing treatment is able to bring the LSPR resonance back for P-doped NCs.

The effect of an annealing treatment on oxidized NCs is shown in Figure 2.3.4b.

Interestingly, the LSPR of oxidized P-doped NCs returns during the annealing treatment, which suggests that defects at the silicon-silicon oxide interface may be reduced due to the low temperature anneal. This is also observed in EPR measurements (see Figure 7.1.7 in Appendix, section 7.1). It should be noticed that the LSPR of annealed P-doped Si NCs is not air stable, but will disappear again slowly, likely due to further oxide formation and the creation of new electron trap states. The annealing of oxidized B-doped Si NCs shows only a minor effect, consistent with our suggestion that defects play only a small role as trap states in B-doped Si NCs.

2.3.4. Modeling plasmonic behavior[1]

Here, we look at a classical hybridization theory and a full quantum mechanical TDLDA approach, developed by collaborators. Due to the band structure of silicon, doping with phosphorus contributes light (transverse) and heavy (longitudinal) electrons, while boron contributes light and heavy holes. The SiNCs are modeled as jellium spheres and a background polarizability of 11.97, as appropriate for bulk Si.[95] Boron (B) doping is hole-type doping and results in holes at the top of the two valence bands at the Γ-point of the Brillouin zone. The effective masses are $m_H = 0.537 m_e$ for the heavy holes and $m_L = 0.153 m_e$ for the light holes where m_e is the mass of a free electron.

[1] Parts of this section were adapted with permission from H. Zhang, R. Zhang, K. S. Schramke, N. Bedford, K. Hunter, U. Kortshagen, P. Nordlander. "Doped Silicon Nanocrystal Plasmonics", ACS Photonics, **2017**, 4, 963–970. Copyright 2017 American Chemical Society.

Phosphorous (P) doping is electron-type doping and results in electrons in the 6 degenerate pockets at the X-points. The anisotropy of these pockets results in two types of carriers with effective masses being $0.916m_e$ for the heavy (longitudinal) and $0.19m_e$ for the light (transverse) electrons.[95] When two carriers of different mass are present, their relative doping densities will be different. For the present B- and P-doping, the relative doping densities are related to the total doping density (n_{Tot}) as

$$n_H = \frac{\left(\frac{m_H}{m_L}\right)^{\frac{3}{2}}}{1+\left(\frac{m_H}{m_L}\right)^{\frac{3}{2}}} n_{Tot},$$

$$n_L = \frac{1}{1+\left(\frac{m_H}{m_L}\right)^{\frac{3}{2}}} n_{Tot},\ n_{Long} = \frac{1}{3} n_{Tot}, n_{Trans} = \frac{2}{3} n_{Tot} \qquad (1)$$

For both P- and B-doping, we will refer to the carriers as heavy (subscript 'H' and 'Long') or light carriers (subscript 'L' and 'Trans'). It makes no difference in the theoretical modeling whether the carriers are electrons or holes or whether the origin of the mass differences is due to band dispersion or anisotropy. Depending on the chemical properties of the dopants and the synthesis process, the dopant distribution in Si NCs can either be primarily bulk, P-doped, or primarily surface doping, B-doped.

The left panels of Figures 2.3.5a and 2.3.5b present the measurements of absorption spectra for the oxidation process of Si NCs under B- and P-doping cases, respectively. Figure 2.3.5c shows the effect of annealing the B-doped Si NCs. The

annealing process can free some trapped carriers to the bulk by passivating dangling bond defects,[42,80] resulting in an increase of free carrier density inside NCs. Figure 2.3.5d shows the effect of fractional precursor flow X_P on the absorbance. To model the measured spectra, we use the doping density and profile as fitting parameters. Annealing results in an increase in carrier densities for both B- and P-doping as charges trapped at the surface become free with increasing temperature.[42,80] The variations of the fitted doping densities in Figures 2.3.5a-d are all consistent with these physical doping mechanisms and align with the experimental data.

The absorption spectra in Figure 2.3.5 exhibit a single resonance. Due to the presence of two different charge carriers, associated with two different plasma frequencies, for both for P- and B-doping, two distinct plasmon resonances might be expected. However, through the calculations of the optical absorption spectra for arbitrary and independent doping concentrations for the different carriers, it was found that the absorption spectra remain characterized by a single plasmon resonance in most cases.

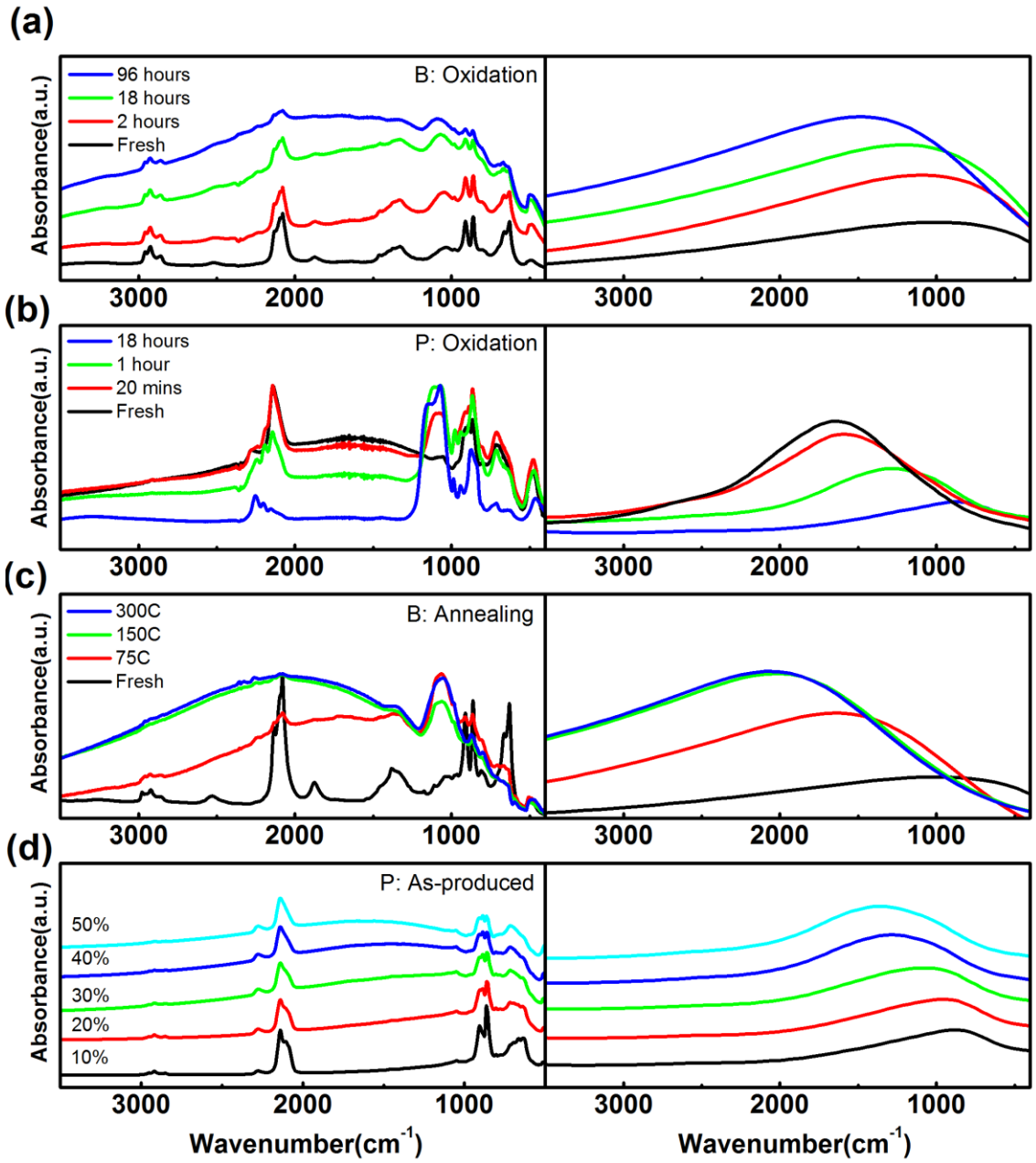

Figure 2.3.5: Measured (left) and calculated (right) absorption spectra. (a) Oxidized B-doped SiNCs ($X_B = 10\%$) for as-produced, 2, 18, and 98-hour oxidization. The fitted doping concentrations are $1.5, 1.9, 2.0, 2.3 \times 10^{20} cm^{-3}$. (b) Oxidized P-doped SiNCs ($X_P = 30\%$) for as-produced, 20-minute, 1-hour, and 18-hour oxidization. The fitted doping densities are $2.1, 2.0, 1.6, 1.1 \times 10^{20} cm^{-3}$. (c) Annealed B-doped SiNCs ($X_B = 10\%$). The fitted doping densities are $1.5, 2.5, 3.2, 3.3 \times 10^{20} cm^{-3}$. (d) As-produced P-doped SiNCs ($X_P = 10, 20, 30, 40, 50\%$). The fitted doping densities are $1.2, 1.3, 1.4, 1.7, 2.0 \times 10^{20} cm^{-3}$. The damping used is $\delta = 0.12$ eV (a, c), 0.04 eV(b,d).

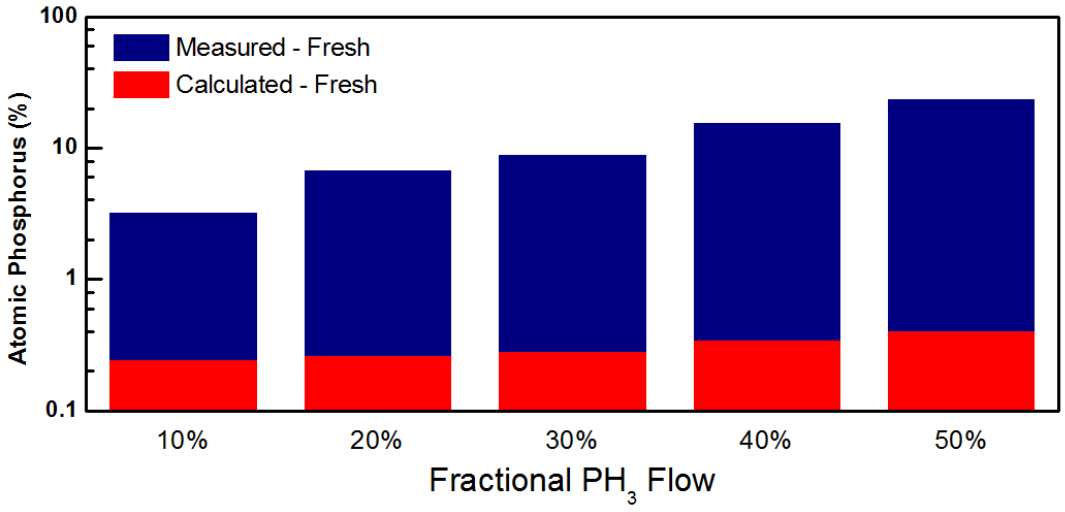

Figure 2.3.6: Comparisons of carrier concentrations of as-produced Si NCs. For each fractional phosphine flow rate (10%to 50%), the height of the blue or red bars shows the measured atomic dopant concentration or fitted doping densities. The fitted carrier concentrations are extracted from calculations of Figure 3.3.2d, where the diameter of the NCs is 8 nm, and the effective masses are 0.916m_e and 0.19m_e.

Figure 2.3.6 summarizes the measured atomic dopant concentration in experiments and the free carrier densities that were extracted from simulations. The measured doping concentrations were determined using energy dispersive x-ray spectroscopy (EDS). The free carrier density is always smaller than the actual atomic concentrations and the ratio of precursors as shown in Figure 2.3.6. This mismatch is due to a substantial amount of inactive dopant atoms at the surface of the nanocrystals.

2.3.5. HE-XRD and RMC Modeling[2]

To further explore whether the dopant distribution may play a role in the absorption spectra, we employed high-energy x-ray diffraction (HE-XRD) coupled to atomic pair

[2] Parts of this section were adapted with permission from H. Zhang, R. Zhang, K. S. Schramke, N. Bedford, K. Hunter, U. Kortshagen, P. Nordlander, "Doped Silicon Nanocrystal Plasmonics", ACS Photonics, **2017**, 4, 963–970. Copyright 2017 American Chemical Society.

distribution function (PDF) analysis[96,97] and reverse Monte Carlo (RMC) structural simulations[49] to experimentally elucidate atomic-scale dopant distribution in the P-doped Si NCs in the form of ensemble average nanoparticle configurations. In this instance, however, the calculated absorption spectra showed no significant dependence on the spatial location of dopant distribution and are all consistent with a bulk dopant profile for as-produced P-doped Si NCs. The plasmonic properties of doped Si nanoparticles are likely affected by the local chemical and structural coordination around the dopant atom, wherein both spatial location of the dopant atom (surface vs. core) and overall structural order directly impacts the local dopant environment. Atomic PDF analysis is an established yet underutilized structure analysis method wherein both Bragg features arising from long-range periodicity and diffuse components originating from a lack of long-range structural order are both simultaneously examined.[96,97] An atomic PDF of 10% P-doped Si nanoparticles is shown in Figure 2.3.7, black line, where peaks in the atomic PDFs represent atomic pair distances with enhanced atomic density. As shown in Figure 2.3.7, red line, RMC simulations reproduce the experimental atomic PDFs reasonably well, with goodness of fit parameters (R_w) below 15%.

An ensemble-averaged nanoparticle configuration was obtained by modeling the atomic PDFs using RMC simulations. RMC simulations do not require any crystallographic information and are only guided by the experimental atomic PDF data and user defined restrictions (nearest neighbor distance, coordination numbers, etc.). As

such, RMC simulations are ideal for structural modeling of inherently disordered systems, including nanomaterials.[98–102] A RMC- generated configuration cross-section is shown in Figure 2.3.8 for 10% P-doped Si NCs. These configurations, modeled directly from experimental structural data, indicate that the nanoparticle has a significantly disordered surface with a more ordered structure within the nanoparticle core which agrees with experimental observations. Using the RMC-generated nanoparticle configuration for the 10% P-doped Si NCs, metrics regarding phosphorus dopant location and coordination can be determined and correlated back to theoretical models and plasmonic properties.

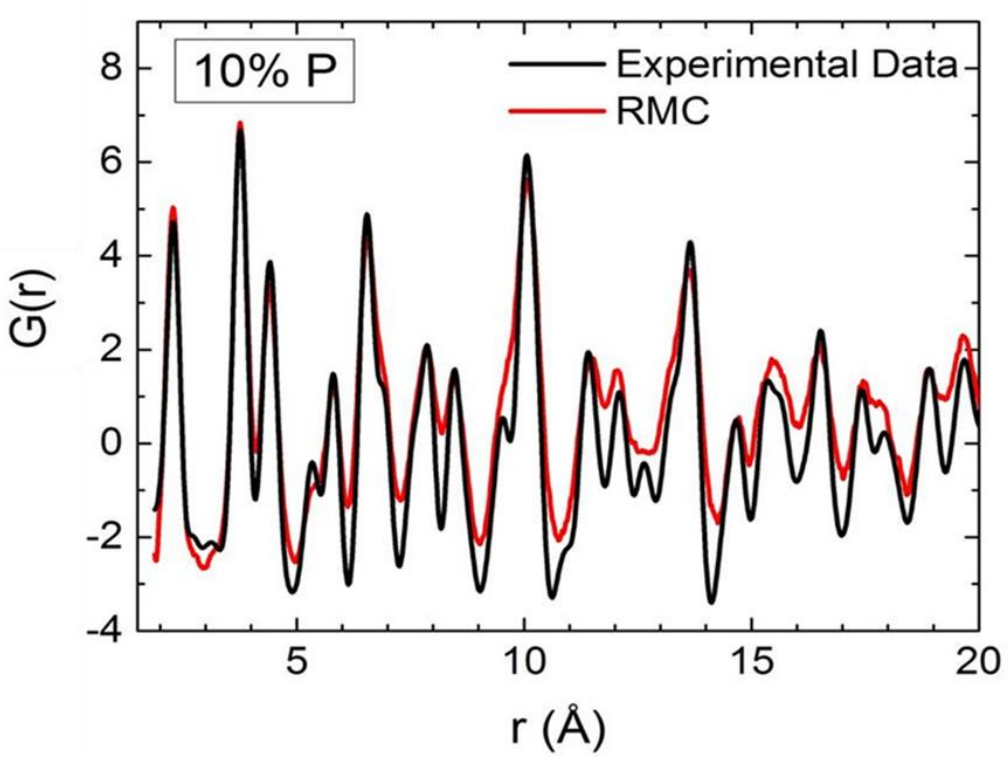

Figure 2.3.7 Atomic PDFs (black line) and corresponding RMC fit (red line) for 10% P-doped nanoparticles.

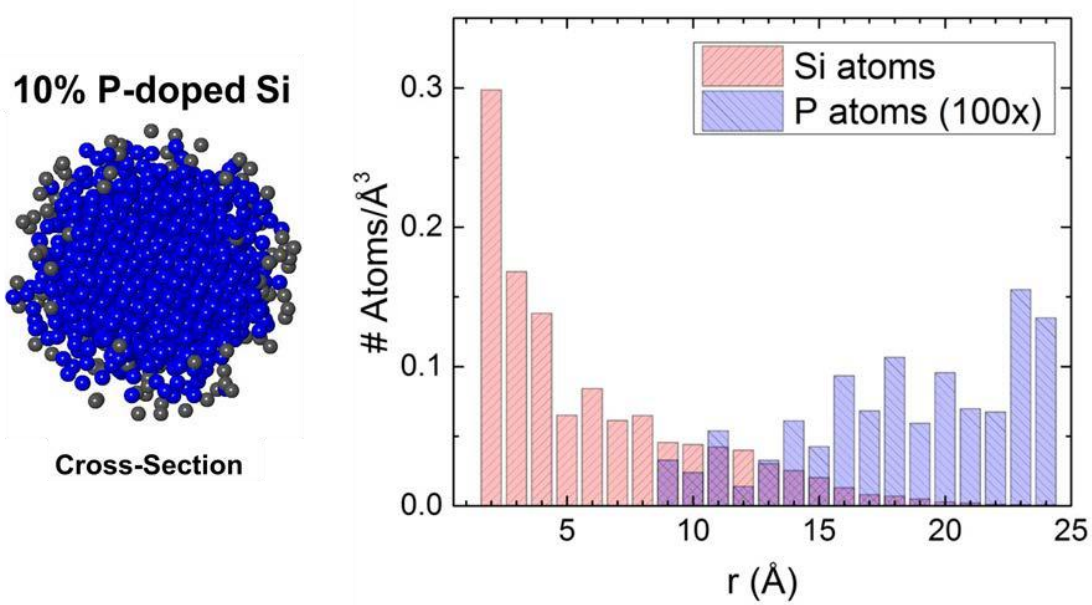

Figure 2.3.8: (Left) Cross section of RMC-generated configuration of 10% P-doped Si nanoparticles. Blue atoms represent Si while grey atoms represent P. (Right) The number of atoms distributed radially from the center of the RMC-generated configuration for 10% P-doped Si nanoparticles, normalized to volume. Red bars represent Si atoms, while blue bars, multiplied by 100x for clarity, represent P atoms.

2.4. Conclusion

Here the plasmonic properties and dopant dynamics of P-doped and B-doped Si NCs that were produced through nonthermal plasma synthesis were studied. While the synthesis and doping method are identical, P-doped and B-doped Si NCs show very different plasmonic behavior which is strongly influenced by their surface properties.

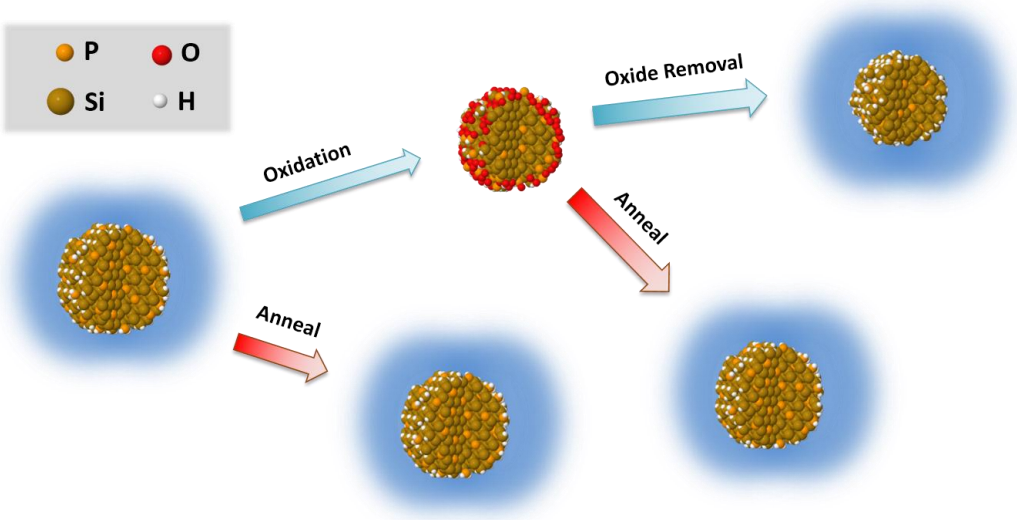

Figure 2.4.1 Summary of the plasmonic behavior of phosphorus doped silicon. The blue clouds around the particles represent plasmonic activity. As-produced phosphorus doped Si NCs, as shown on the far left, are plasmonic and remain plasmonic, with an increase in active carriers, when annealed at low temperatures. The LSPR diminishes and disappears with oxidation but appears again with removal of the oxide layer or low temperature annealing. The presence of an LSPR begins for phosphorus doped silicon after ~10% nominal doping and blue-shifts with increased nominal doping up to 50%.

P-doped Si NCs exhibit an LSPR as-produced but this quickly disappears upon oxidation, Figure 2.4.1. This is consistent with substitutional doping that produces free electrons, which are trapped as defects at the silicon-silicon oxide interface develop upon oxidation. This interpretation is supported by EPR measurements, which indicate the generation of P_b centers. XPS also shows a decrease of the number of tetravalent phosphorus as a silicon oxide shell grows. Annealing at low temperatures restores the plasmonic response, likely due to remediation of defect sites due to hydrogen diffusion.

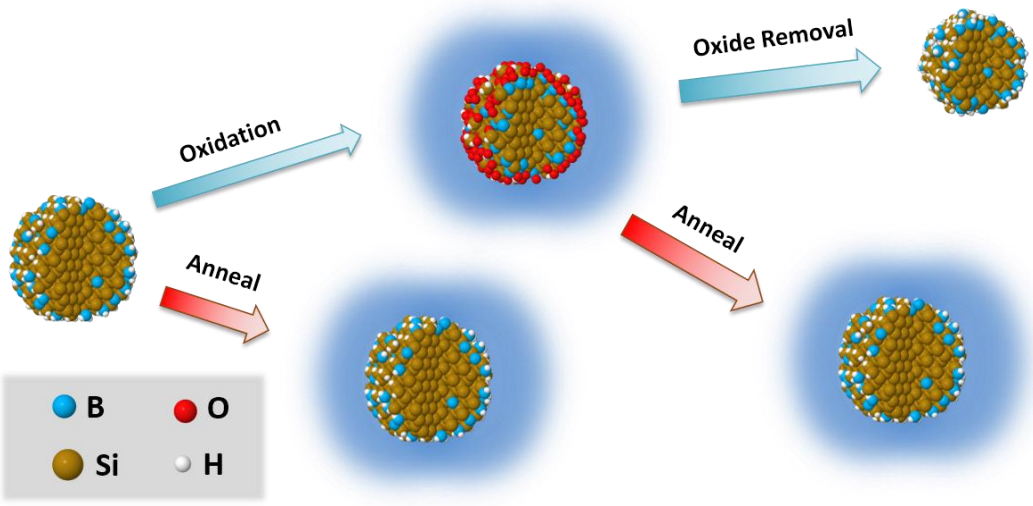

Figure 2.4.2 Plasmonic behavior of B-doped silicon nanocrystals. The blue clouds around the particles represent plasmonic activity. As-produced boron doped Si NCs are not plasmonically active. Post-synthesis treatments of both oxidation and annealing activate the LSPR. Oxide removal returns the NCs to their as-produced state.

B-doped Si NCs exhibit no LSPR as-produced but develop plasmonic response upon oxidation, Figure 2.4.2. EPR measurements suggest that B-doped Si NCs have a very low defect density, which does not increase upon oxidation. Hence trap states seem to be of little importance for B-doped Si NCs. Moreover, XPS measurements show very minor changes in the number of trivalent and tetravalent boron dopants. This behavior suggests a lesser role of substitutional doping by boron, but it is consistent with surface doping. While we currently do not fully understand the underlying mechanism, we suggest boron-oxide species at the Si NC surfaces as candidates for electron acceptors. Further work is needed to clarify the doping mechanism and quantum chemical calculations may be helpful to elucidate the role of different surface species.

It is important to note that the B-doped Si NCs show environmentally stable LSPRs after complete oxidation. Strong plasmonic behavior is observed for samples that have been exposed to air at ambient conditions for more than a year. Air stability is an important result for the application of Si NCs as infrared plasmonic materials.

2.5. Experimental Methods

Nanoparticle synthesis: Silicon nanocrystals are synthesized in a continuous-flow, low-pressure plasma reactor from an argon-silane (SiH_4) gas mixture. Dopants are introduced by addition of phosphine (PH_3) or diborane (B_2H_6) to the gas mixture. The reactor consists of a borosilicate glass tube through which the reactant gases are flown. Typical flow rates are 30-50 standard cubic centimeters per minute (sccm) of argon, 0.4-0.6 sccm of silane, 0-2 sccm of diborane diluted in hydrogen (10%) and 0-2 sccm of phosphine diluted in hydrogen (15%). Radio frequency (rf) power is supplied at 110 W and 13.56 MHz to ring electrodes to form crystalline silicon nanoparticles in the plasma. The NCs are collected directly onto glass substrates, silicon wafers, or aluminum-coated silicon wafers and transferred air-free to a nitrogen-purged glovebox using a push-rod assembly.

Fourier transform infrared spectroscopy (FTIR) experiments were conducted in either a nitrogen-purged glovebox or directly in air using a Bruker Alpha FTIR spectrometer in DRIFTS mode or transmission mode. Spectra were collected by

averaging 20 scans at 2 cm^{-1} resolution.

Hydrofluoric acid (HF) vapor etching (50% in water) of oxidized Si NCs was performed in a room-temperature container. The oxide was removed after exposing the Si NCs to the vapor for 2 to 4 hours. After etching, the samples were transferred air-free to a nitrogen- purged glovebox for further analysis.

X-ray Photoelectron Spectroscopy (XPS) spectra are acquired on a Surface Science Laboratories, Inc. SSX-100 XPS with a monochromatic Al Kα x-ray source. A x-ray power of 200 W with a 1 mm spot size was used. Si NC samples are prepared by directly impacting a <50 nm thin film of Si NCs onto a gold-coated Si wafer. B1s and P1p peaks were obtained by integrating scans for 2.5 hours. Peaks are assigned by using the C1s peak as a reference at 285 eV.

Electron Paramagnetic Resonance (EPR) measurements were taken using a Bruker Continuous Wave Elexsys E500 electron paramagnetic resonance spectrometer. For the measurements, a few milligrams of Si NC powder was carefully loaded into the bottom of sample tubes (suprasil quartz), and the open end of the tubes was sealed with epoxy glue in order to enable their transport from the glovebox to the EPR spectrometer without exposing the NCs to air. The spectra were normalized to the weight of the nanoparticles.

X-ray Diffraction (XRD) from nanoparticles was collected using a Bruker-AXS Microdiffractometer with a 2.2 kW sealed Cu x-ray source. The nanoparticle diameter is calculated from the Scherrer equation.

Transmission Electron Microscope (TEM) images of the doped nanoparticles were collected on lacy-carbon grids and examined with a Tecnai G2 F30 transmission electron microscope.

Energy Dispersive X-ray Spectroscopy (EDX) data was collected using a JSM-6610LV SEM with an Oxford Instruments Inca X-Act EDS system. Doped Si NCs were deposited on conductive carbon tape for atomic concentration measurement.

Plasmon modeling was completed by Hui Zhang and Runmin Zhang in Professor Nordlander's group at Rice University.

HE-XRD patterns were obtained by Nick Bedford, at the 11-ID-B beamline of the Advanced Photon Source, Argonne National Laboratory using 58.66 keV irradiation. Nanoparticles were loaded into 2.0 mm outer diameter quartz x-ray capillaries, sealed under inert atmosphere, then loaded into NMR tubes which were subsequently flame sealed to prevent nanoparticle oxidation. X-ray capillaries were loaded into NMR tubes such that the x-ray capillary was centered in the middle of the NMR tube using Teflon tape. The sample to detector distance was calibrated using CeO_2 powder loaded in a similar geometry. HE-XRD patterns were collected using an area detector in a transmission geometry to Q_{max} = ~30 $Å^{-1}$. HE-XRD patterns were corrected for background scattering, converted into S(Q), and Fourier transformed into PDFs using the program RAD.[103] Briefly, the raw HE-XRD data was background corrected and converted into their corresponding total structure functions S(Q). The atomic pair

distribution functions, G(r), were obtained from the Fourier transform of Q[S(Q)-1]. The atomic PDF is defined as $G(r) = 4\pi r(\rho(r) - \rho(0))$, where r is the distance between two atom pairs, $\rho(r)$ is local atomic density, and $\rho(0)$ is the average atomic density.

RMC Modeling. To obtain nanostructure configurations and local P and B structural information, atomic PDFs were modeled with reverse Monte Carlo (RMC) simulations using RMC++.[104] A 5 nm truncated ideal Si crystal served as starting configurations for RMC simulations. 10% of the Si atoms were randomly replaced with P to reflect the nominal doping from the nanoparticle synthesis. Constraints in the RMC simulations included minimum Si-Si and Si-P bond length distances. Additionally, ~10% of RMC generated moves allowed for Si-P position swaps to prevent initial structure biasing of the simulations. The 5 nm size was used erroneously since the actual nanocrystals were closer the 7.75 nm in size (size distribution information shown in Appendix 7.1). This could potentially influence the results of the RMC modeling.

2.6. Acknowledgement

The work of N.J.K. and U.R.K. was supported by the DOE Plasma Science Center for Predictive Control of Plasma Kinetics. The work of K.S.S. and U.R.K. was supported by the Army Office of Research under MURI Grant W911NF-12-1-0407. Part of this work was carried out in the College of Science and Engineering Characterization Facility, University of Minnesota, which has received capital equipment

funding from the NSF through the UMN MRSEC program under Award Number DMR-1420013. Part of this work also used the College of Science and Engineering Minnesota Nanocenter, University of Minnesota, which receives partial support from NSF through the NNIN program.

3. Synthesis of Faceted, Large Phosphorus Doped Silicon Nanocrystals

3.1. Introduction

Employing a constricted filamentary plasma has been previously shown to have a significant effect on nanocrystal growth within the plasma.[105] This work revealed that highly faceted Si NCs can be grown to large sizes, 40+ nm in diameter, when grown within a constricted, filamentary plasma with a residence time of several seconds.[105] These large nanocrystals are of particular interest for their potential use in single particle electronic devices including transistors or floating gate memory devices.[105,106] These NCs also allow for the possibility of examining their structural properties, such as the elastic limit, as the relatively large facets provide a location to apply a force to induce deformation.[107] Structural properties, just like electronic properties, of nanomaterials can vary greatly from the bulk properties.[108–110] These properties remain largely unstudied for many materials. Large, faceted doped silicon nanocrystals are also of interest to compare the nanocrystalline properties of doped silicon to that of intrinsic silicon and could be useful for similar electronic device applications.[111,112] Due to the inherent safety issues imposed by working with the dopant gases, diborane (B_2H_6) or phosphine (PH_3) – both of which are pyrophoric and highly toxic at the parts per million level, this experiment could not be completed in the same plasma reactor used to produce the Si

nanocubes. In this work, I endeavored to develop experimental conditions that would yield 20-100 nm faceted P-doped Si NCs.

3.2. Results and Discussion

The nonthermal plasma synthesis process affords several controls over experimental design, though some are tied into one another. Residence time, or the amount of time a nanocrystal spends within the plasma, directly correlates to the size of the nanocrystal.[7] The target residence time is several seconds for this type of nanocrystal growth.[105,107] The relationship for residence time is described most simply by $t_{res} = \frac{V_{plasma}}{Q \times P}\ [s]$ where t_{res} is the residence time, V_{plasma} is the volume of the plasma, Q is the flow rate, and P is the chamber pressure. The plasma volume is the simplified part of this equation since it can be changed by altering the electrode position however this can also affect the plasma properties. For this work the electrode spacing is defined as the distance from the bottom of the top copper ring electrode to the top of the stainless steel ultraTorr fitting at the base of the reactor tube. Adjusting the flow rate also changes the pressure, which can be accounted for by adjusting the width of the downstream nozzle.

Beyond these general controls, we can also adjust the recipe for the NCs and the input power. The silane (SiH_4), on this system is 100% so no additional gas needs to be accounted for when adjusting its flow, however the PH_3 is diluted to 15% in hydrogen.

The additional hydrogen can be significant as it can etch particle surfaces within the plasma and is sometimes injected into the plasma to control the surface of the NCs.[113,114] The first step was then to find conditions that would yield a constricted filamentary plasma followed by determining the significance of the available variables. I found that the nominal input power had to be at least 110 W and the SiH_4 flow rate had to be kept below 0.3 sccm to induce instabilities in the plasma. Then the effects on morphology of electrode spacing, input power, argon flow, and PH_3 flow were studied. The 8 sets of experimental conditions are described in Table 1.

Table 1: Synthesis conditions for faceted NC experiment.

Figure	Electrode Spacing (cm)	Nominal Power (W)	Argon Flow (sccm)	SiH_4 Flow (sccm)	PH_3 Flow (sccm)	P (%)
3.1	6.5	110	9.6	0.3	0.36	15
3.2		130				
3.3	5	130	9	0.25	0	0
3.4	5.8					
3.5	5				0.18	10
3.6	5.8					
3.7			10			
3.8			11			
3.9	6.5		9.6			

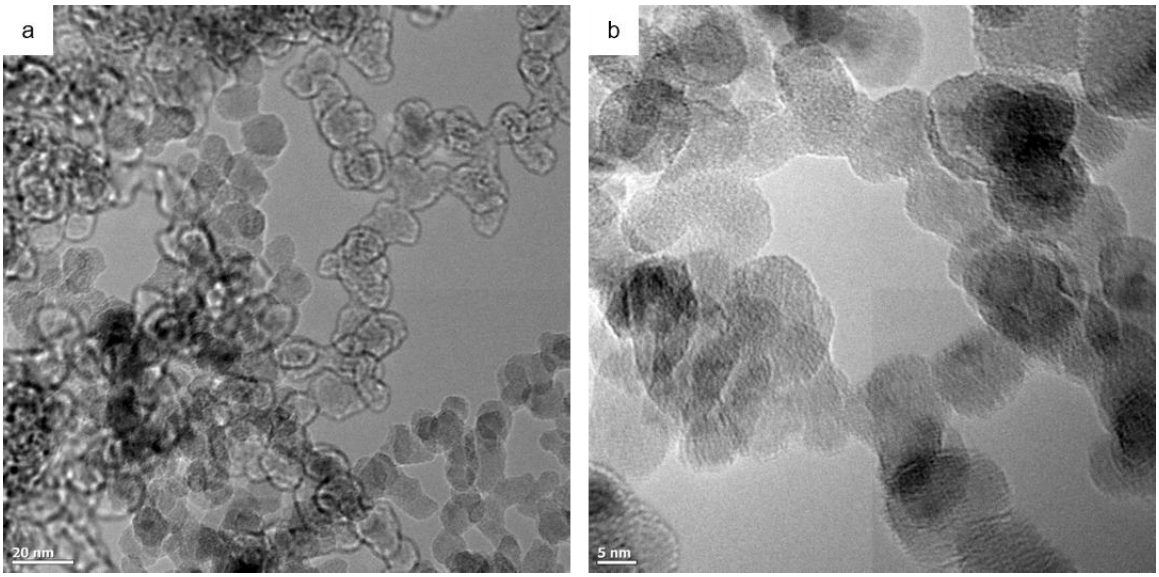

Figure 3.2.1 TEM images of sample 1 with scale bars of (a) 20 nm and (b) 5 nm synthesized at 110 W, 15% P-doping, argon flow of 9.6 sccm, and electrode spacing of 6.5 cm.

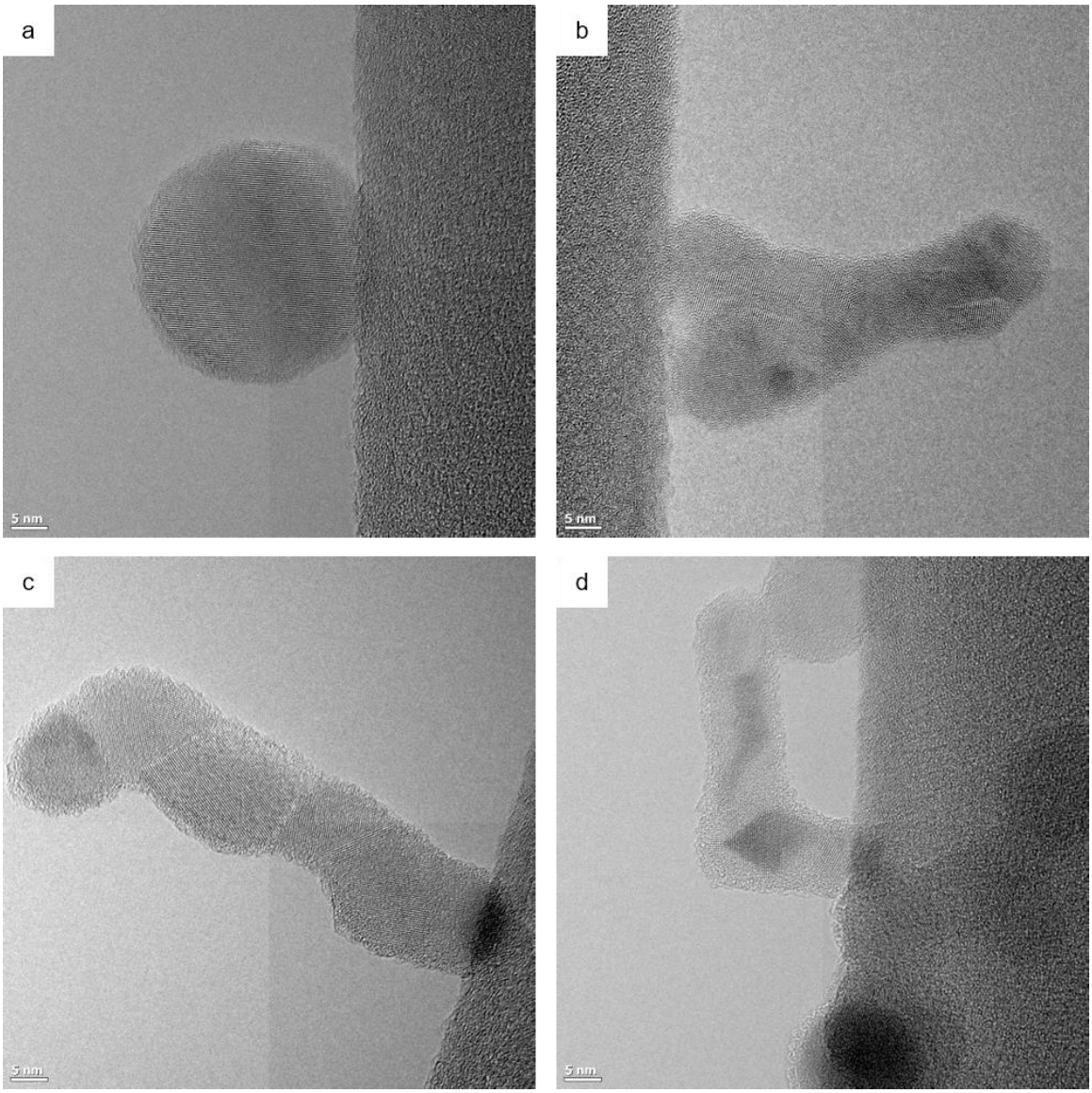

Figure 3.2.2: TEM images of sample 2 with scale bars of 5 nm synthesized at 130 W, 15% P-doping, argon flow of 9.6 sccm, and electrode spacing of 6.5 cm.

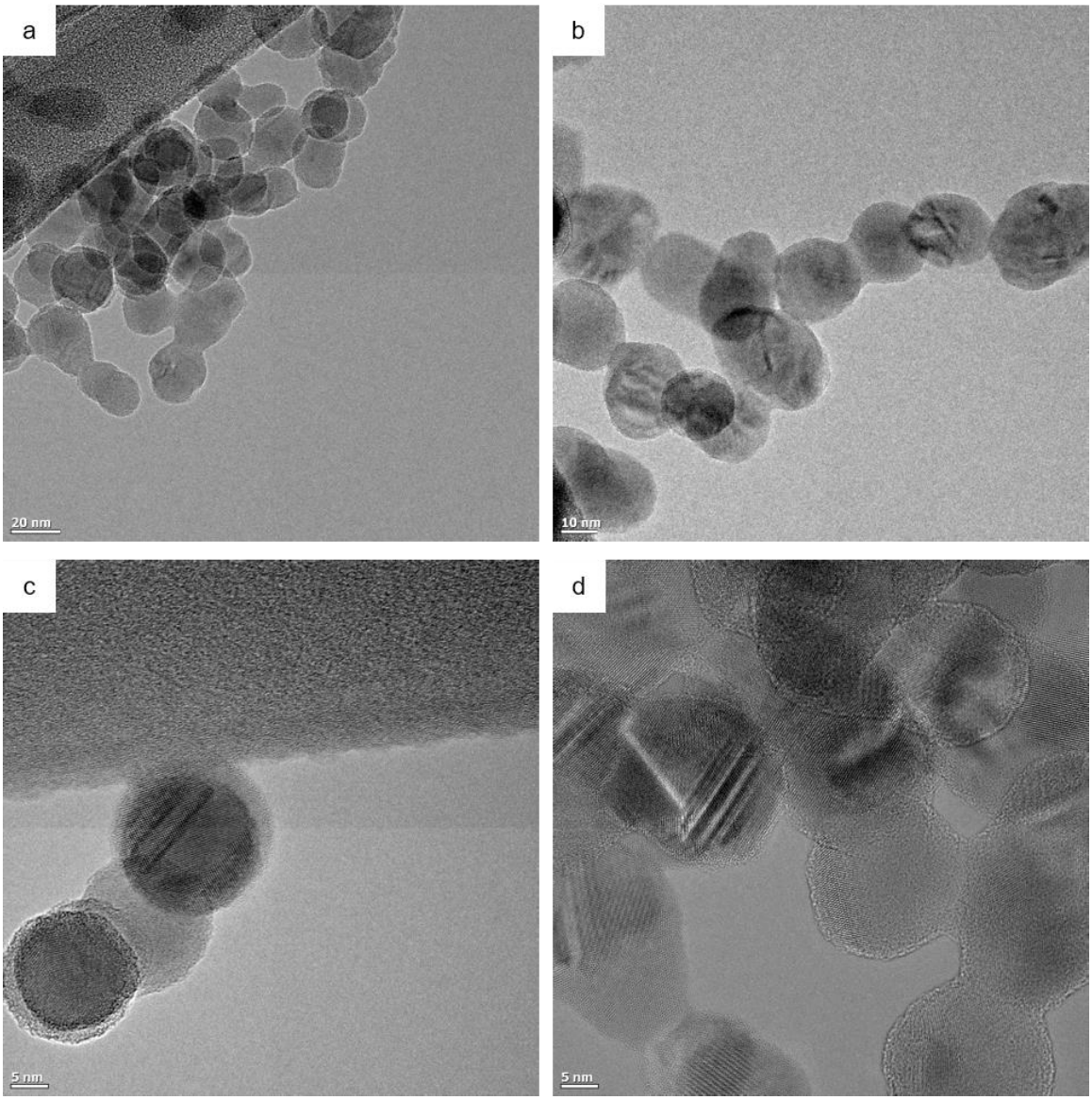

Figure 3.2.3: TEM images of sample 3 with scale bars of (a) 20 nm, (b) 10 nm, (c) 5 nm, and (d) 5 nm synthesized at 130 W with no P-doping, argon flow of 9.0 sccm, and electrode spacing of 5.0 cm.

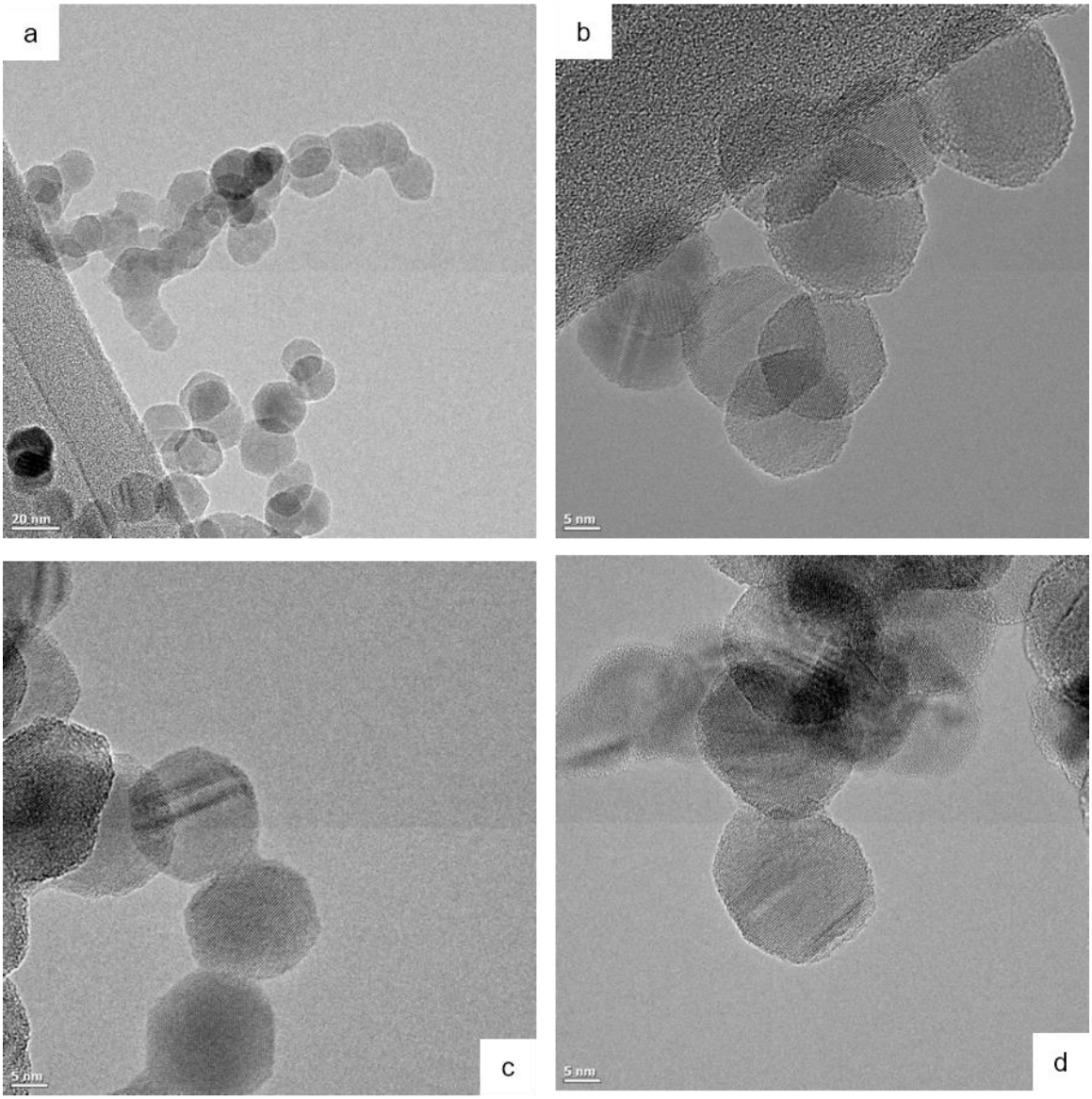

Figure 3.2.4 TEM images of sample 4 with scale bars of (a) 20 nm, (b) 5 nm, (c) 5 nm, and (d) 5 nm synthesized at 130 W with no P-doping, argon flow of 9.0 sccm, and electrode spacing of 5.8 cm.

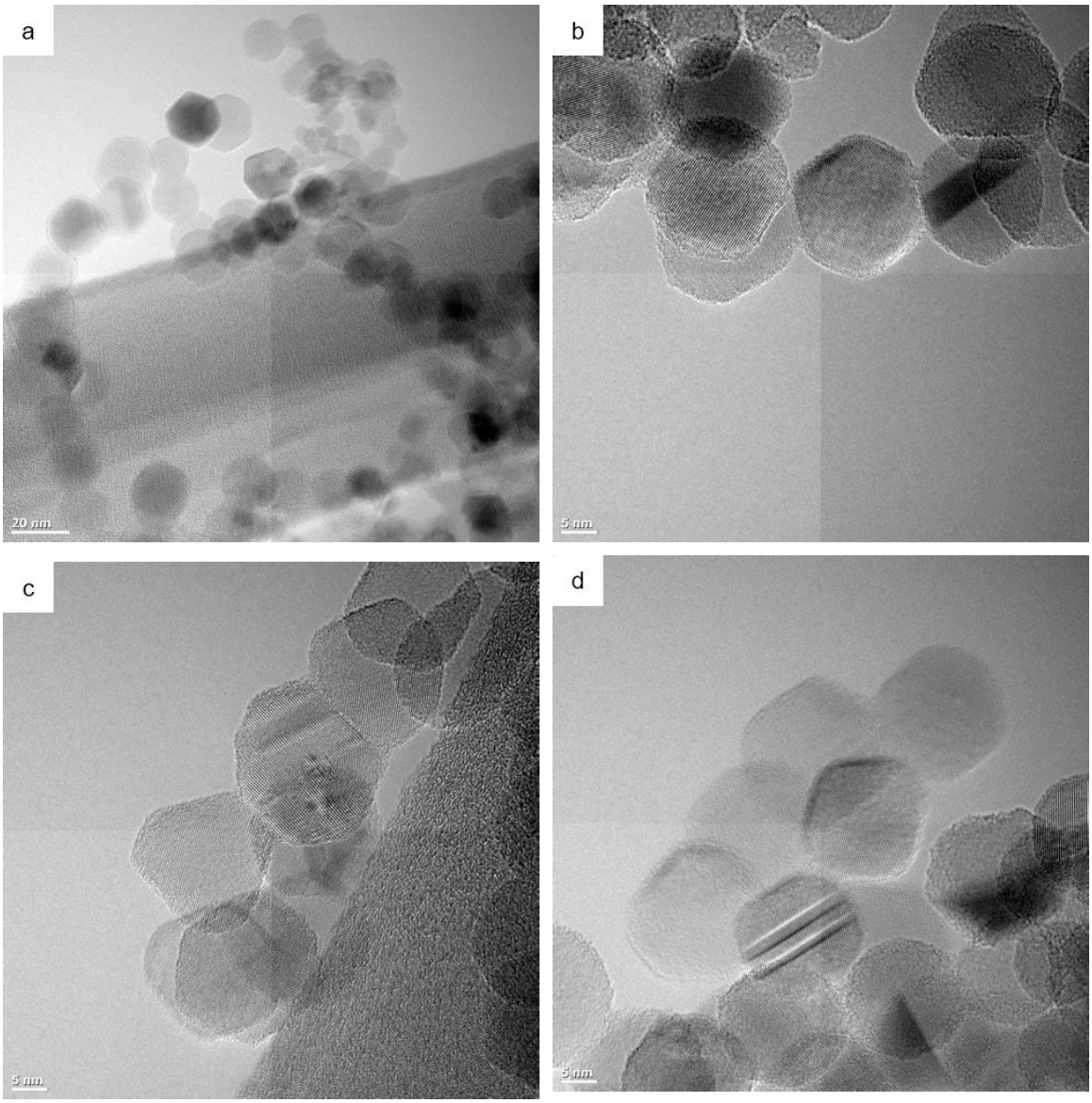

Figure 3.2.5: TEM images of sample 5 with scale bars of (a) 20 nm, (b) 5 nm, (c) 5 nm, and (d) 5 nm synthesized at 130 W with 10% P-doping, argon flow of 9.0 sccm, and electrode spacing of 5.0 cm.

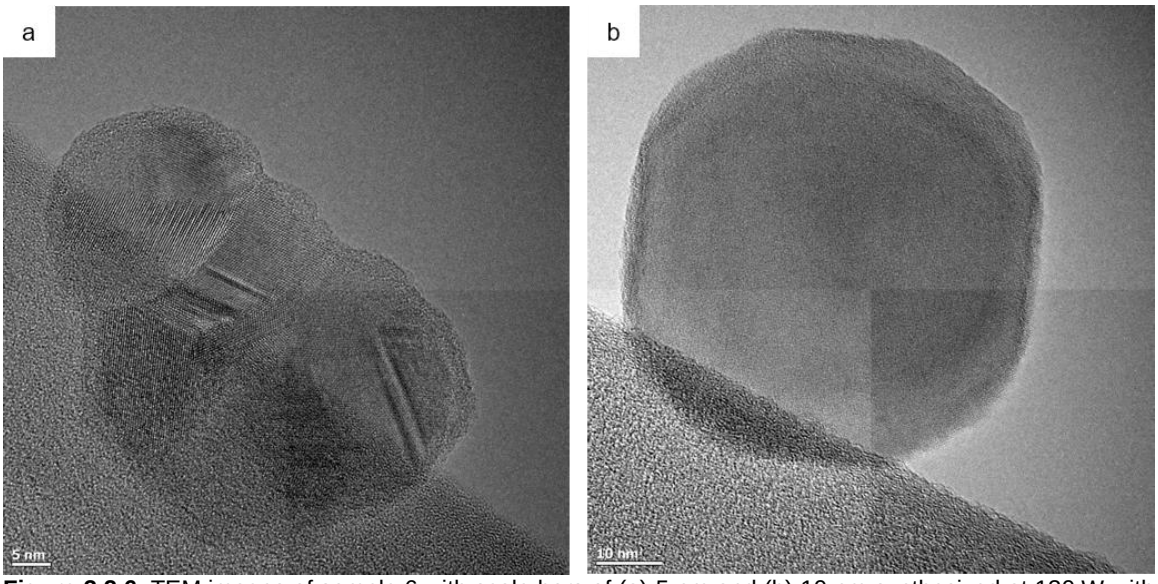

Figure 3.2.6: TEM images of sample 6 with scale bars of (a) 5 nm and (b) 10 nm synthesized at 130 W with 10% P-doping, argon flow of 9.0 sccm, and electrode spacing of 5.8 cm.

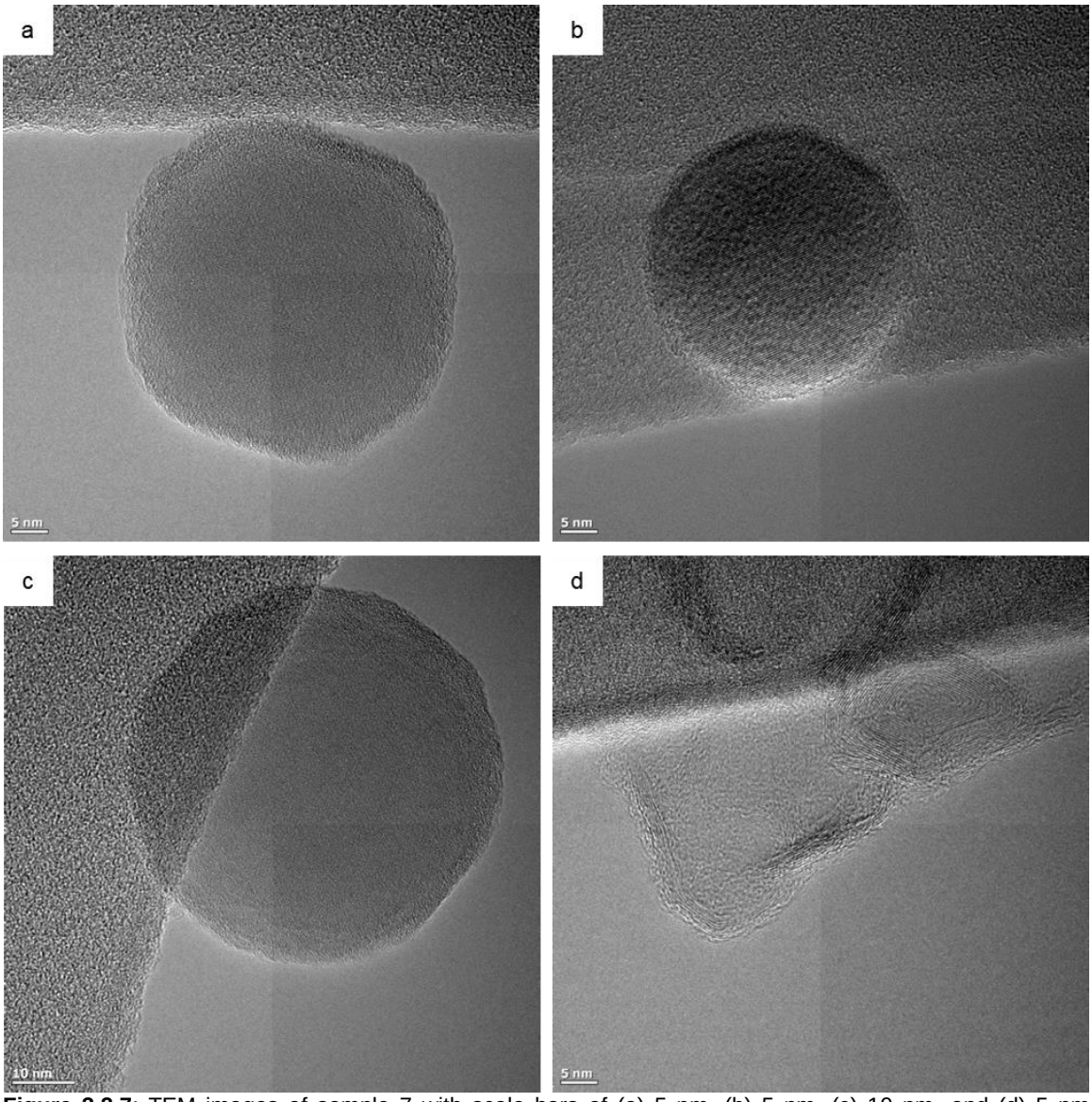

Figure 3.2.7: TEM images of sample 7 with scale bars of (a) 5 nm, (b) 5 nm, (c) 10 nm, and (d) 5 nm synthesized at 130 W with 10% P-doping, argon flow of 10.0 sccm, and electrode spacing of 5.8 cm.

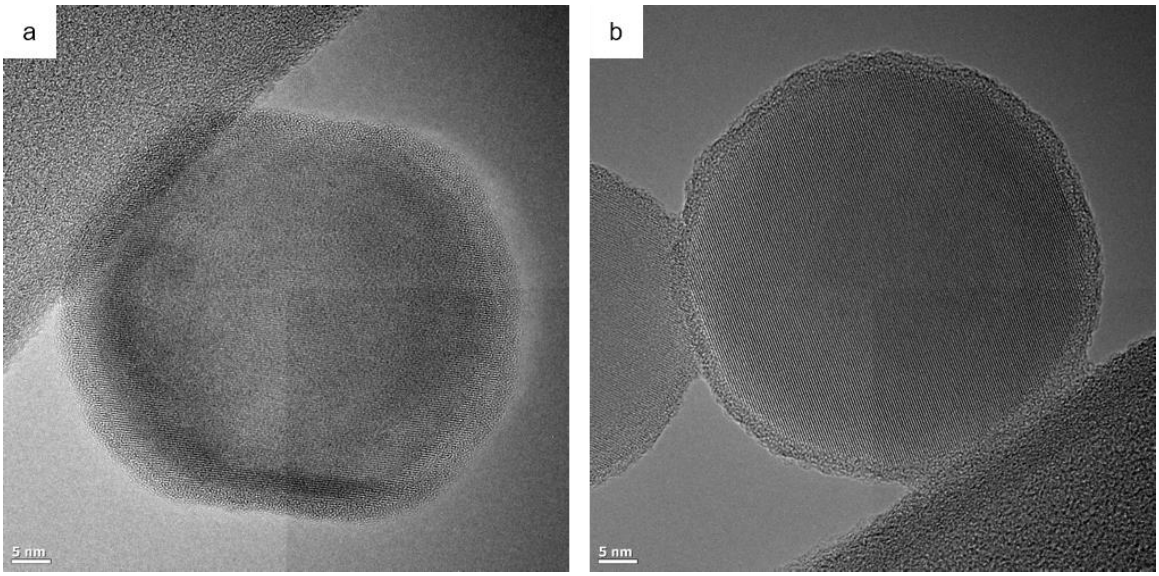

Figure 3.2.8: TEM images of sample 8 with scale bars of 5 nm synthesized at 130 W with 10% P-doping, argon flow of 11.0 sccm, and electrode spacing of 5.8 cm.

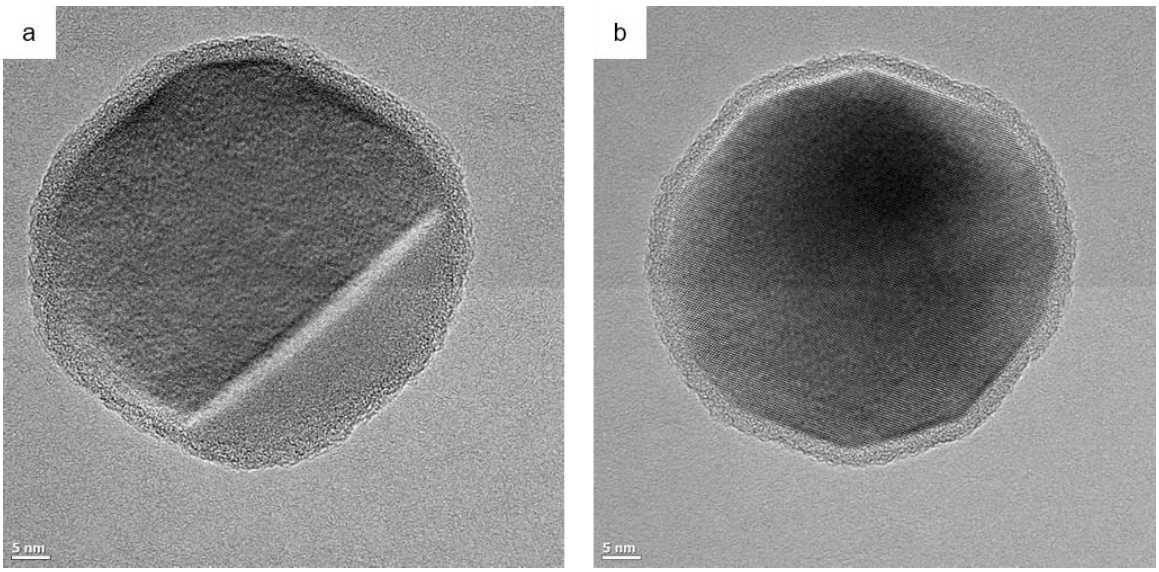

Figure 3.2.9: TEM images of sample 9 with scale bars of 5 nm synthesized at 130 W with 10% P-doping, argon flow of 9.6 sccm, and electrode spacing of 6.5 cm.

3.2.1. Input Power

Figures 3.2.1 and 3.2.2 can be compared to see the effect of input power on the NCs. The NCs in Figure 3.2.1, synthesized at 100 W, are around 10 nm in diameter and irregularly shaped with no obvious crystal lattice diffraction. The plasma was unstable but not consistently filamentary, just intermittent flickers in an otherwise diffuse plasma. With the increase in nominal power to 130 W the plasma filaments still flickered but at a much higher frequency with the filaments consistently visible during synthesis. The NCs in Figure 3.2.2 change drastically from the NCs shown in Figure 3.2.1, now with obvious crystal lattice diffraction. The morphology is different as well with the formation of compound structures made up of several 5-10 nm crystallites twinned together, shown in Figures 3.2.2b-d. The formations appear to be random with no obvious preferential behavior. In addition to these multi-crystallite structures, there are some spherical particles that appear to be single crystals approximately 30 nm in diameter with a 1 nm amorphous shell, Figure 3.2.2a. This shows that higher power and a filamentary plasma yields larger crystalline NCs which is consistent with previous work.[6,105]

3.2.2. Electrode Spacing

The electrode spacing was varied from 5 cm to 6.5 cm over the course of the study. The effect of electrode spacing can be examined by comparing samples 3 and 4 which are intrinsic silicon as well as samples 5 and 6 produced with 10% P-doping, both shifting from an electrode spacing of 5 cm to 5.8 cm. This change in electrode spacing

accounts for a ~16% increase in plasma volume. Figures 3.2.3 c-d and 3.2.4 c-d all have linear ridges in some of the particles which could be from a grain boundary. Samples 3 and 4 both have ~20 nm average diameter. Sample 4, with larger electrode spacing, has slightly more faceted NCs. Figure 3.2.5 shows elongated spheroidal NCs (Figures 3.2.5 a,b and d), some hexagonal shaped particles (Figure 3.2.5a), and some tetrahedral particles (Figure 3.2.5d) while Figure 3.2.6 has octahedral NCs. Again, both samples have thick ridge-like features, Figures 3.2.5c-d and 3.2.6a. There is the presence of twinning and disordered multi-crystalline structures in Figures 3.2.5c and 3.2.6a.

For this set of samples, the difference between the presence of PH_3 or lack thereof is more interesting than the electrode spacing difference which is minimal. The effect of PH_3 will be discussed in the following section.

3.2.3. Phosphine Flow

Now we can take a closer look at Figures 3.2.4 and 3.2.5 and the difference caused by adding PH_3 into the reactor during synthesis. Figure 3.2.5 shows mostly faceted particles of relatively monodispersed size distribution. Figure 3.2.4 shows particles that are only slightly faceted. This is likely due to the additional hydrogen present in the plasma with the PH_3, which is known to etch NC surfaces within the plasma. With a long enough residence time the NCs are etched preferentially along certain crystal planes.[105]

Figure 3.2.2 and Figure 4.2.9 show two sets of particles where the differences are the percentage of P-doping, 15% and 10% respectively, and sample 9 was made with a lower SiH_4 flowrate. The single crystalline NCs in Figure 3.2.9 are close in size to the NC shown in Figure 3.2.2a, but more faceted and with a thicker amorphous shell. This agrees with previous observations of additional hydrogen present with the higher PH_3 flow helps etch away some of that amorphous shell leaving a cleaner NC surface.

3.2.4. Argon Flow

Looking at Figures 3.2.6, 3.2.7, and 3.2.8, the effect of argon flow on the NCs is minimal. All three sets of particles are of comparable size and morphology. As expected, there is no significant effect on the amorphous outer layer or crystallinity. The resulting change in residence time from the pressure change due to the varied flow rates was not significant enough to change the particle size.

3.3. Conclusion

The presence of additional hydrogen from increased PH_3 flow and the presence of the constricted filamentary plasma proved to be the most significant factors in forming faceted NCs in this plasma reactor. Argon flow and electrode spacing did not have a notable effect on the NCs. Figure 3.2.9 shows the most promising particles for future study. To further improve the NC properties, power could be increased and a hydrogen source separate from the dopant gases could be added to the system. That way, hydrogen

injection and doping percentage could be independently controlled to optimize the synthesis process.

3.4. Experimental Methods

The nanocrystals were produced using the same experimental set-up described previously in Chapters 2 and 3. Argon, 100% SiH_4, and 15% PH_3 in H_2 were the precursors used for these experiments. The downstream orifice used was circular and 1mm in diameter. Synthesis pressure remained in the range of 1.5-2 Torr. The nanocrystals were deposited directly on TEM grids that were adhered to glass slides with a very small amount of carbon tape. It could be useful to note here that handling of TEM grids can be difficult since they are very delicate and prone to jumping away at the slightest presence of small breezes and static electricity. This is the reason that there are only two, rather than three data points for some sections.

TEM images were taken by Eric Hintsala using the Tecnai G2 F30 transmission electron microscope. The TEM grids were transferred air-free in the push-rod assembly from the reactor to the glovebox where the grids were transferred to a grid box and placed in a small vacuum container. The samples were exposed to oxygen during transfer to the TEM for measurement.

4. Nonthermal Plasma Synthesized Titanium Nitride with Gold-like Plasmonic Behavior

4.1. Introduction

Titanium nitride (TiN) is of interest due to its plasmonic properties which are compatible with photothermal therapy treatments as well as its physical properties. Gold is one of the most common plasmonic materials and gold nanorods are currently the most applicable for photothermal therapy treatments (PTTs). In order for a material to be useful for these types of biological applications, it must absorb within the biological transparency window, from 650 to 1350 nm.[30,31,115] Plasmonic metal nanomaterials have localized surface plasmon resonances (LSPRs) that depend strongly on their size, shape, and morphology. A gold nanosphere has an LSPR peak around 500 nm while gold nanorods with varied aspect ratios have resonances that shift into the near infrared where the biological transparency window lies.[30,116] However, gold nanorods deform at relatively low temperatures and a minor change in nanorod aspect ratio leads to significant changes in plasmonic properties which can result in ineffective material.[117,118] TiN is also a potential candidate for use as an obscurant. Obscurants are used to block out specific regions of the electromagnetic spectrum in a controlled manner.

Colloidal synthesis techniques, as used for gold nanorods, include multiple processing and temperature sensitive steps, involve numerous chemicals, and generate

chemical waste.[115,118,119] Nonthermal plasma synthesis of nanomaterials is a continuous production process that also minimizes material waste and eliminates lengthy processing steps which are inherent to colloidal synthesis methods.[7,120,121]

TiN nanoparticles have a localized surface plasmon resonance that already lies in the biological transparency window[122–125] so additional morphology manipulation is not necessary as it is with growing gold nanorods.[20,118,119] At the time this paper was written, to the author's knowledge, only one other instance of plasmonic TiN nanoparticles synthesized via nonthermal plasma has been shown.[124] The TiN nanoparticles produced in the previous work required a post-synthesis heating step to remove ammonium salts which formed due to the interaction between the ammonia and chlorine in the titanium precursor.[124]

4.2. Results and Discussion

4.2.1. Size and Crystallinity

The deposition rate of NCs for this process is close to 1 mg/minute and the produced NCs were approximately 5 nm in diameter as confirmed by transmission electron microscopy (TEM) and selected area diffraction (SAD), Figure 4.2.1 – left panel. Additional characterization of the particles with the TITAN, Figure 4.2.1 – right panel, shows that the NCs are polycrystalline, made up of 1-2 nm crystallites twinned together in the 5 nm particles. This suggests that the growth mechanism within the plasma is different from previously studied semiconductor plasma synthesized particles.

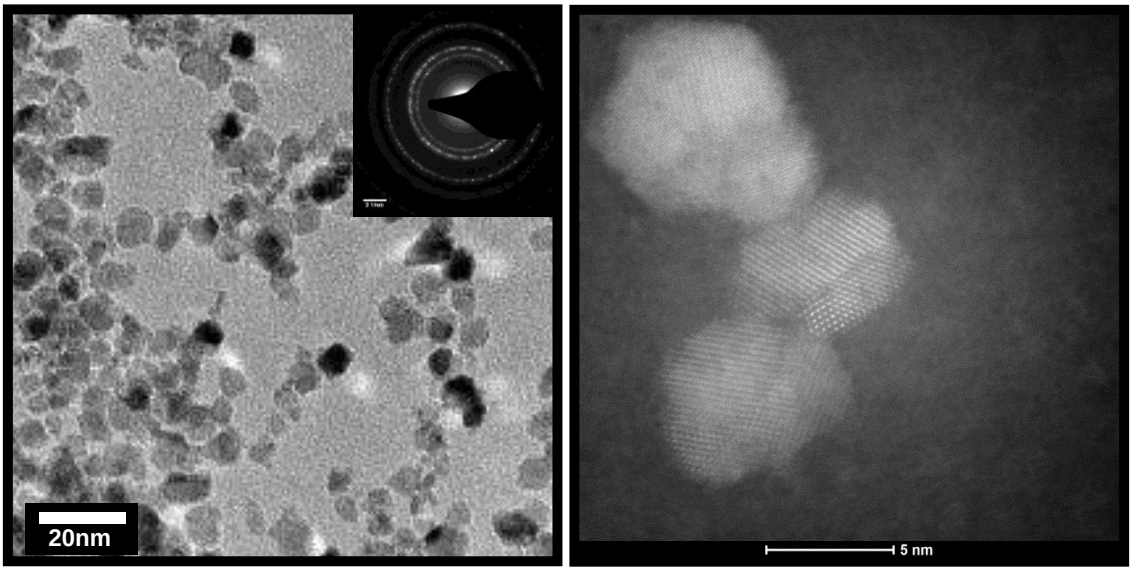

Figure 4.2.1: (Left) TEM image (taken by Yunxiang Qin) shows the uniform distribution of ~5 nm TiN nanoparticles. (Right) Titan TEM image (taken by Jacob Held) showing well defined lattice fringes indicating the polycrystallinity of the TiN particles.

Initial power studies showed an increase in crystallinity of the TiN NCs with increased power using x-ray diffraction (XRD). The particle size measured by XRD is not impacted significantly by synthesis power or ammonia flow, however, the polycrystallinity may make XRD a less reliable measure of particle size (See Appendix 7.3 for XRD plots).

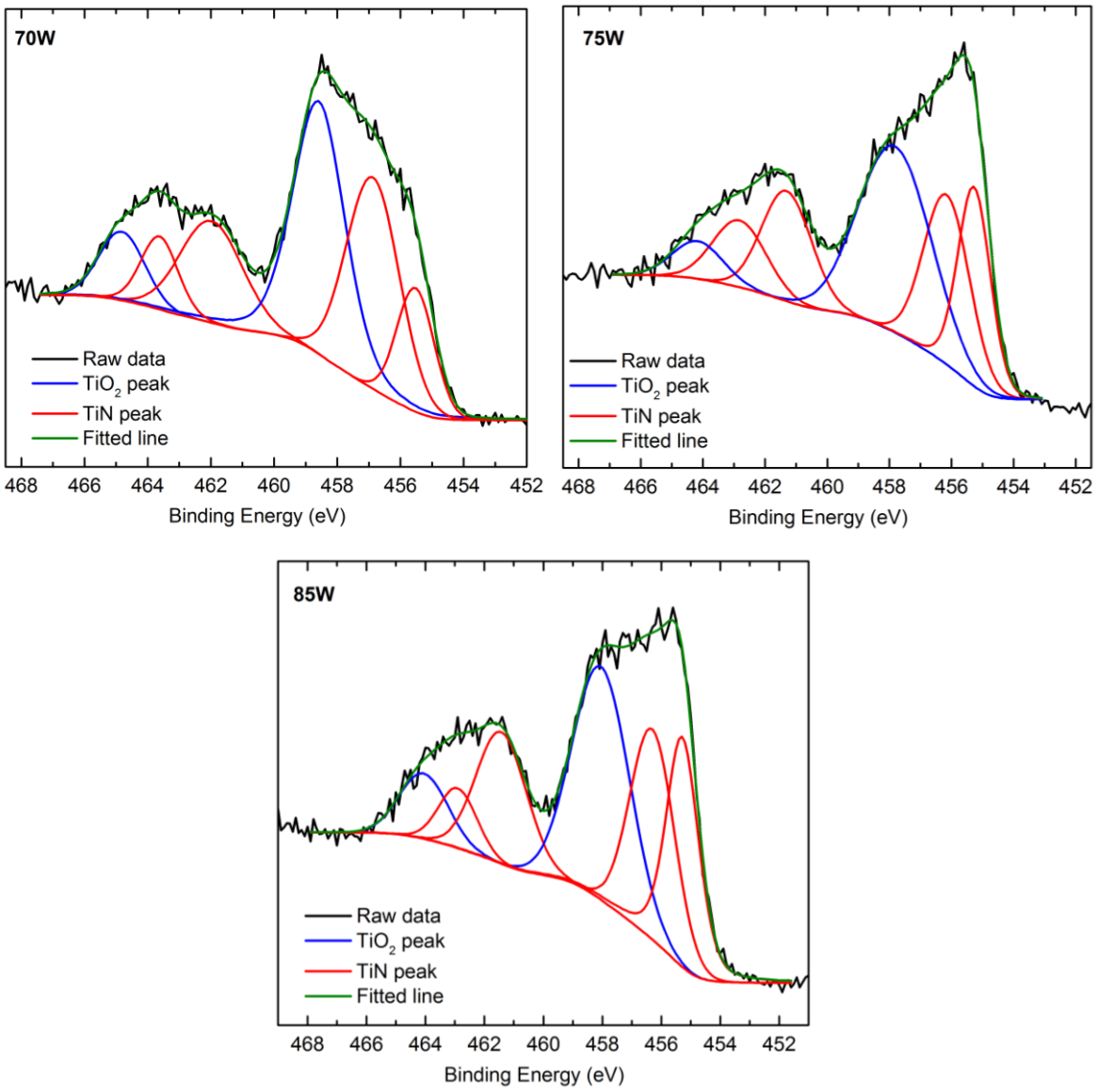

Figure 4.2.2: High resolution XPS scans of the Ti 2p peak of TiN samples made at nominal powers of 70W – 63% of bonds are from TiN and 37% are from TiO_2, 75W – 60%/40% TiN/TiO_2, and 85W – 62%/38% TiN/TiO_2. The blue peaks at 464 eV and 458 eV are from titanium bonded to oxygen and the red peaks at 463 eV, 461.5 eV, 456.3 eV, and 455.3 eV are from titanium bonded to nitrogen.

4.2.2. Elemental Composition and Morphology

Nonthermal plasma produced nanoparticles of various materials have crystalline core and up to a nanometer of amorphous surface.[7] The elemental composition of the TiN nanoparticles was measured using x-ray photoelectron spectroscopy (XPS). Survey scans confirm the presence of titanium, nitrogen, carbon, and oxygen (shown in Appendix 7.3). The carbon comes from the methyl groups in the titanium precursor. The TiN particles were consistently nitrogen rich and the particles exhibiting the strongest LSPR had two nitrogen atoms for every titanium atom. High-resolution XPS scans of the titanium peak were fitted to find that TiN NCs tend to have ~40% of titanium atoms bonded to oxygen atoms and ~60% bonded to nitrogen atoms (Figure 4.2.2). This suggests that the titanium located at the disordered surface of the nanoparticle readily oxidizes to form titanium dioxide. Assuming a stoichiometric TiN crystalline core, supported by XRD peak locations and TEM/Titan images, this leaves surplus, beyond what is in the TiN core, nitrogen and carbon near the surface of the particles. The amount of carbon and surplus nitrogen is enough to form several disordered atomic layers at the surface of a 5 nm nanocrystal core.

Fourier transform infrared spectroscopy (FTIR) measurements were made to examine this hypothesis and to see what bonds are present at the TiN NC surface. As can be seen in Figure 4.2.3, the FTIR spectrum of the NCs confirms the existence of several

carbon and nitrogen bonds at the measurable sample surface. The hydrogen bonds shown in the FTIR come from the methyl groups from the metalorganic titanium precursor.

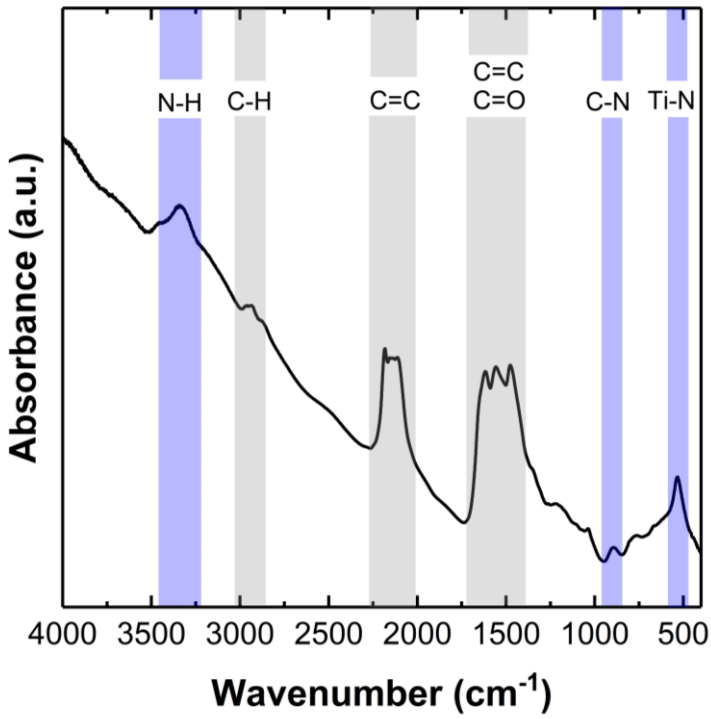

Figure 4.2.3: FTIR of TiN NCs with peaks from N-H[126,127], C-H[128], C=C[127,129], C=O[130], C-N[128], and Ti-N[129] bonds at the surface of the NCs.

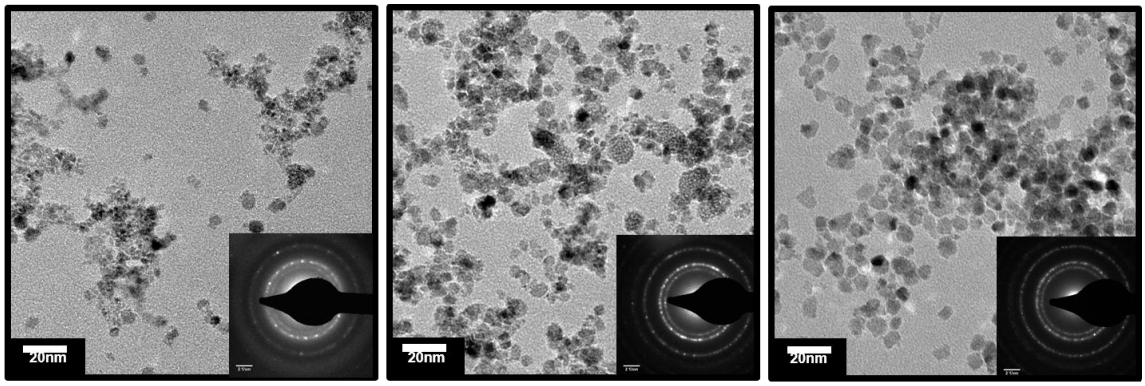

Figure 4.2.4: TEM images (taken by Yunxiang Qin) of TiN NCs with the ammonia flow rate for synthesis of these samples increase, left to right, from 0.3 sccm to 1.2 sccm.

Ammonia flow greatly affects the morphology, composition, and properties of the TiN NCs. At very low ammonia flow rates, the morphology varies significantly, there are few larger NCs and many smaller non-uniform nanocrystalline structures, Figure 4.2.4 – left. As ammonia flow rate is increased the NC morphology becomes more uniform and the non-uniform structures begin to disappear leaving a wide size distribution of nanoparticles, Figure 4.2.4 – center, then with more ammonia, monodispersed tetrahedral 5 nm nanoparticles, Figure 4.2.4 – right. Carbon content decreases from ~40% to ~25% with increase in ammonia flow and the Ti:N ratio decreases with a similar trend over the same flow range (shown in Appendix 7.3). A similar decrease in carbon content with increased ammonia flow has previously been observed in atmospheric pressure chemical vapor deposition (APCVD) of TDMAT.[131] This could suggest that the hydrogen in the ammonia has an etching effect on the carbon containing surfaces of the nanocrystals and perhaps the smaller, non-uniform structures have a high carbon content as well.

4.2.3. Absorption

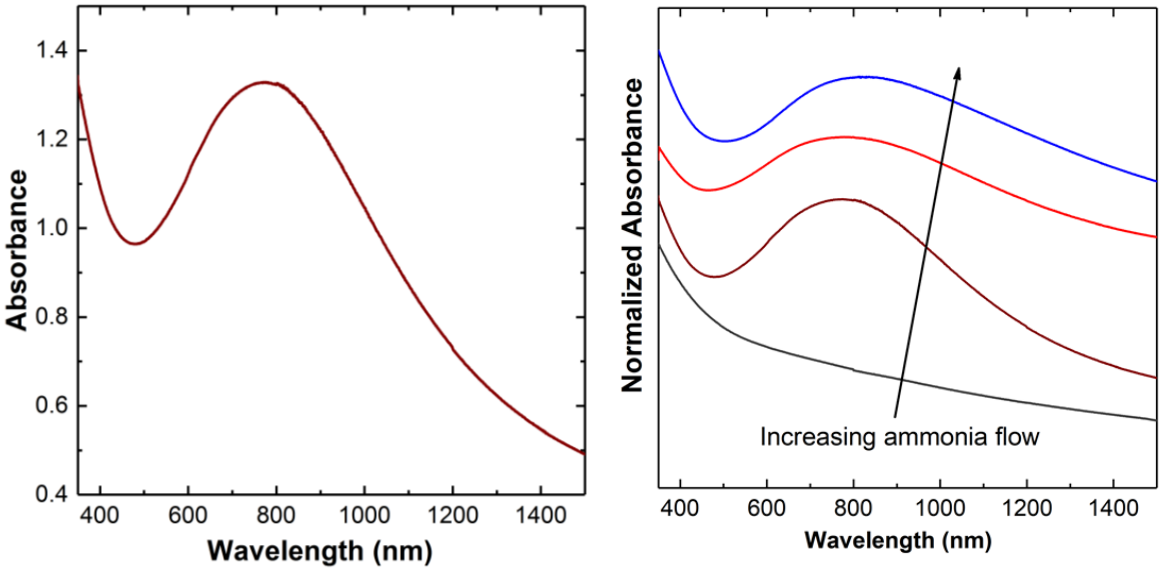

Figure 4.2.5: UV-Vis spectra showing the LSPR of the TiN NCs, (left) single spectrum showing the actual absorbance and (right) stacked spectra showing the change in LSPR with ammonia flow increasing from 0.3 sccm where no plasmon is observed to 3.0 sccm where a broadened plasmon is observed.

The LSPR of the TiN NCs was measured using UV-Visible absorption spectroscopy. The NCs have a plasmon resonance in the range of 770-800 nm which is within the biologic transparency region, making the TiN conducive to PTTs, Figure 4.2.5 – left. Figure 4.2.5 – right panel shows the change in LSPR with ammonia flow. At very low ammonia flow rates no LSPR is present and as ammonia flow is increased, the plasmon appears, then broadens and slightly redshifts. The broad size distribution and nonuniformity of the NCs produced with 0.3 sccm of ammonia is not favorable for a plasmon resonance. Obscurant properties are also of interest for this material and absorption measurements were conducted by NanoComposix on the TiN NCs. The TiN

NCs have similar performance to the TiO_2, the current industry standard for obscurants (Shown in Appendix 7.3). This is promising and could certainly be studied further.

4.2.4. Solution dispersion

The TiN NCs dispersed reasonably well into chloroform and water forming a cloudy solution when agitated by hand and forming a more transparent solution after sonication. The solutions were not stable as the particles would crash out of solution within 24 hours. Further work could be done to improve the dispersibility of the TiN NCs. Figure 4.2.6 shows the TiN NCs dispersed in water on the left and the TiN NCs deposited directly on the substrate on the right.

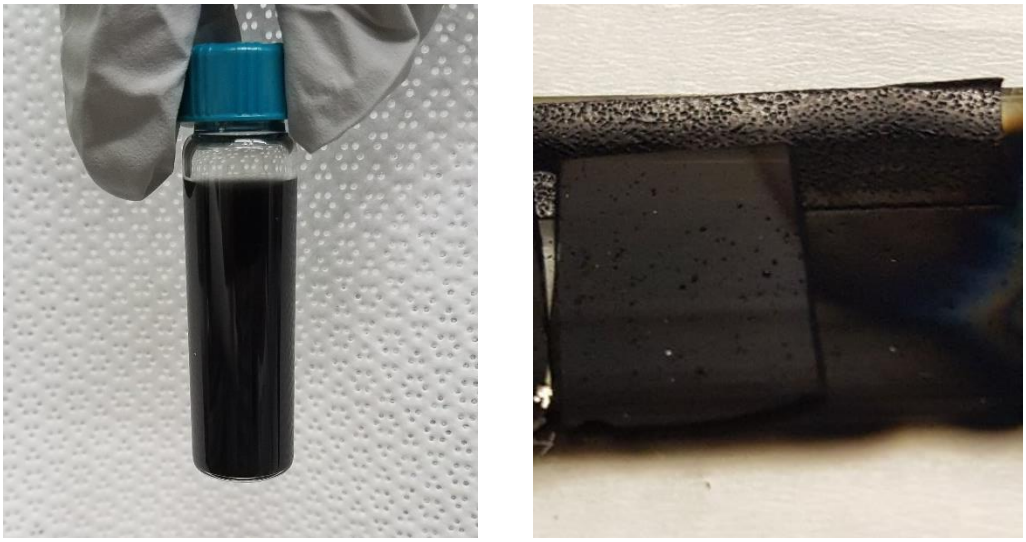

Figure 4.2.6: (left) TiN NCs dispersed in water and (right) an example of TiN NC film deposition on a glass slide and aluminum coated silicon wafer.

4.3. Conclusion

Plasmonic TiN NCs were successfully synthesized via nonthermal plasma synthesis using a metalorganic titanium precursor for the first time. The absorbance of the TiN NCs make them a candidate for use as an obscurant. The observed LSPR was in a similar location to that of the gold nanorods suitable for PTT applications. Nanoparticle uniformity and optimized elemental compositions are required for good plasmonic behavior. An ammonia flow of 1.2 sccm proved to be the best experimental condition for the LSPR which has a narrower shape than the previously reported LSPR for plasma-produced TiN. The width and presence of the LSPR is dependent on the ammonia flow rate as is the uniformity and composition of the NCs.

4.4. Experimental Methods

The TiN nanoparticles were synthesized utilizing a nonthermal plasma process during which the gaseous or aerosolized precursors are injected into an argon plasma where the nanoparticles nucleate and grow. Figure 4.4.1 shows a schematic of the plasma reactor used for TiN synthesis. It is the same general setup that has been previously described for the productions of doped silicon nanocrystals but has some differences, most significantly, the precursors. In these experiments, a metal-organic precursor, tetrakis(dimethylamido)titanium (TDMAT), commonly used as an atomic layer deposition or chemical vapor deposition precursor[132–135], was used as the titanium

precursor. The TDMAT is contained in a stainless-steel bubbler and argon is flowed through the TDMAT to carry it to the plasma reactor. Due to the low vapor pressure of the metalorganic liquid, the TDMAT process lines and bubbler were heated to 80°C and 70°C respectively to prevent condensation inside the reactor or lines. Ammonia was used as a nitrogen precursor to allow additional control over nitrogen content. It is still unclear how the TDMAT molecule breaks down within the plasma and whether the nitrogen within the molecule can be utilized for crystal growth.

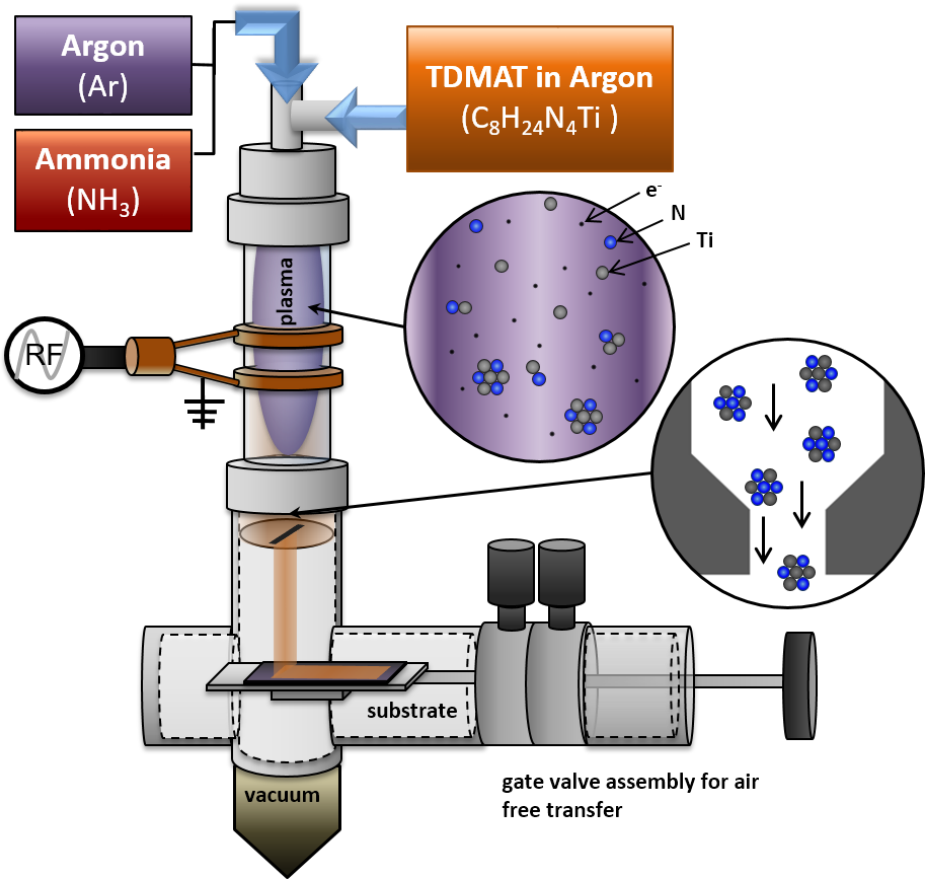

Figure 4.4.1: The experimental setup for TiN NC synthesis. Argon, ammonia, and TDMAT carried by argon are the precursors used for the synthesis of TiN NCs. The dimensions of the downstream nozzle used in all experiments are 10 mm x 0.610 mm. Synthesis pressure was ~1.6 Torr.

FTIR experiments were conducted in either a nitrogen-purged glovebox or directly in air using a Bruker Alpha FTIR spectrometer in DRIFTS mode. IR spectra were collected by averaging 20 scans at 2 cm^{-1} resolution. NCs were deposited directly onto aluminum coated silicon wafer and transferred in the pushrod assembly to the nitrogen filled glovebox for FTIR measurement.

UV-Vis measurements were made on the Cary UV-Vis-NIR spectrophotometer located in Eray Aydil's laboratory. The particles were deposited directly onto glass for the measurements. The prepared samples were taken in air from the lab in ME L126 to the lab, Amundson G6, for measurement. The samples were exposed to air for varied amounts of time, up to several days, before UV-Vis measurements were taken but air exposure did not have a noticeable effect on the absorption properties.

XPS spectra were acquired on a Surface Science Laboratories, Inc. SSX-100 XPS with a monochromatic Al Kα x-ray source. A x-ray power of 200 W with a 1 mm spot size. The Ti 2p high resolution peaks were collected by integrating scans for 30 minutes. The peaks were assigned using the C1s peak as a reference at 285 eV. NCs were deposited directly onto silicon wafers for this measurement. The NCs were transferred in air from the lab to the characterization facility for XPS measurement.

XRD from nanoparticles was collected using a Bruker D8-Discover with a Co x-ray source. The nanoparticle diameter was calculated from the Scherrer equation. NCs were

deposited directly onto glass and transferred in air for this measurement.

TEM images of the doped nanoparticles were collected on and examined with a Tecnai G2 F30 transmission electron microscope by Yunxiang Qin or the FEI Titan transmission electron microscope by Jacob Held. NCs were deposited directly onto carbon-coated 400-mesh Cu TEM grids from Ted Pella Inc and transferred in air to the characterization facility for measurement.

5. Summary and Proposed Work

LSPRs of nonthermal plasma synthesized nanoparticles have been studied in this work for both their potential applications as well as a diagnostic tool in the case of doped silicon. The impact of experimental conditions on the physical and optical properties of nonthermal plasma synthesized nanocrystals was examined. A better understanding of phosphorus and boron dopant behavior in silicon in both as-produced and post-synthesis treated NCs and experimental conditions for plasmonic TiN was obtained.

Plasmonic behavior in doped silicon was used as an indicator of dopant activity and found that phosphorus and boron behave very differently within the plasma synthesized Si NCs. We further studied the dynamics of the dopants using high energy XRD and RMC modeling of the pair distribution functions. This, along with the theory models of plasmonic behavior has solidified the hypothesis that the doping profile of boron differs from that of phosphorus. For this synthesis process, boron dopants tend to be located at or near the surface where oxidation places a key role in dopant activation while active phosphorus dopants tend to be located uniformly throughout the nanocrystal. Both B-doped and P-doped Si NCs benefit, from a dopant activation standpoint, by the passivation of surface defects caused by low temperature annealing.

The RMC simulation models produced from the PDFs obtained from HE-XRD are very promising and could unveil a lot of information about dopant behavior in our Si

NCs. There is a current collaboration between myself and Katharine Hunter and Nick Bedford. This collaboration will be continued by Katharine Hunter. We are currently studying the possibility of dopant diffusion as a result of low-temperature annealing. The experiment design includes injecting dopant precursor into the afterglow of the plasma to have dopants only at or near the NC surface. The PDFs and RMCs of the NC samples before and after annealing will be compared and examined for evidence of dopant relocation. This is a current work in progress and we do not yet have enough results to make any conclusions. This work can be continued going forward to advance the knowledge of P and B dopants in Si as well as in germanium.

The experimental controls were studied and large, faceted P-doped Si NCs were produced. A synthesis recipe for the desired NC properties was established. This is the first instance, to the knowledge of the author, that P-doped SiNCs of this size and morphology have been produced via nonthermal plasma. Going forward, these NC's structural properties could be analyzed in the same way the Si nanocubes were previously. This would be a good opportunity to be trained on the NanoIndenter in the Minnesota Nanocenter. Additionally, these experiments could be extended to include B-doped NCs allowing the physical properties of nanocrystalline P-doped and B-doped Si to be compared.

This work has also shown that TiN has plasmonic properties conducive for use in photothermal therapy treatments. Although the LSPR of the nonthermal plasma synthesized TiN is in the correct location for biological applications, more work is needed for this material to be used in the human body. The absorbance within the biological transparency window causes photothermal materials to heat up when irradiated. The TiN should be measured to find out how efficiently and what temperature it will reach when irradiated. TiN is already a known bio-compatible material used as a coating for implants but studies with TiN nanoparticles will be needed. It is also likely that other transition metal nitrides, particularly zirconium nitride which has garnered some interest, could be useful alternatives to gold and silver for plasmonic applications.

To pursue the obscurant application, the production process should be scaled up from 1 mg/minute. The measurement methods for obscurant materials require a minimum of 100 mg to perform. This could be done by building a new reactor specifically for TiN synthesis and allowing for higher flow of TDMAT and additionally, utilizing a mesh bag collection method to more efficiently collect the particles.

6. Bibliography

(1) Yin, Y.; Alivisatos, A. P. Colloidal Nanocrystal Synthesis and the Organic–inorganic Interface. *Nature* **2005**, *437*, 664–670.

(2) Talapin, D. V; Lee, J.-S.; Kovalenko, M. V; Shevchenko, E. V. Prospects of Colloidal Nanocrystals for Electronic and Optoelectronic Applications. *Chem. Rev.* **2010**, *110*, 389–458.

(3) Littau, K. A.; Szajowski, P. J.; Muller, A. J.; Kortan, A. R.; Brus, L. E. A Luminescent Silicon Nanocrystal Colloid via a High-Temperature Aerosol Reaction. *J. Phys. Chem.* **1993**, *97*, 1224–1230.

(4) Ehbrecht, M.; Huisken, F. Gas-Phase Characterization of Silicon Nanoclusters Produced by Laser Pyrolysis of Silane. *Phys. Rev. B* **1999**, *59*, 2975–2985.

(5) Pratsinis, S. E. Flame Aerosol Synthesis of Ceramic Powders. *Prog. Energy Combust. Sci.* **1998**, *24*, 197–219.

(6) Kramer, N. J.; Anthony, R. J.; Mamunuru, M.; Aydil, E. S.; Kortshagen, U. R. Plasma-Induced Crystallization of Silicon Nanoparticles. *J. Phys. D. Appl. Phys.* **2014**, *47*, 75202.

(7) Mangolini, L.; Thimsen, E.; Kortshagen, U. High-Yield Plasma Synthesis of Luminescent Silicon Nanocrystals. *Nano Lett.* **2005**, *5*, 655–659.

(8) Kramer, N. J.; Schramke, K. S.; Kortshagen, U. R. Plasmonic Properties of Silicon Nanocrystals Doped with Boron and Phosphorus. *Nano Lett.* **2015**, *15*, 150727103119001.

(9) Gresback, R.; Holman, Z.; Kortshagen, U. Nonthermal Plasma Synthesis of Size-Controlled, Monodisperse, Freestanding Germanium Nanocrystals. *Appl. Phys. Lett.* **2007**, *91*.

(10) Anthony, R.; Thimsen, E.; Johnson, J.; Campbell, S.; Kortshagen, U. A Non-Thermal Plasma Reactor for the Synthesis of Gallium Nitride Nanocrystals. *Mater. Res. Soc. Symp. Proc.* **2006**, *892*, 5–8.

(11) Felbier, P.; Yang, J.; Theis, J.; Liptak, R. W.; Wagner, A.; Lorke, A.; Bacher, G.; Kortshagen, U. Highly Luminescent ZnO Quantum Dots Made in a Nonthermal Plasma. *Adv. Funct. Mater.* **2014**, *24*, 1988–1993.

(12) Mubeen, S.; Lee, J.; Singh, N.; Krämer, S.; Stucky, G. D.; Moskovits, M. An Autonomous Photosynthetic Device in Which All Charge Carriers Derive from Surface Plasmons. *Nat. Nanotechnol.* **2013**, *8*, 247–251.

(13) Sil, D.; Gilroy, K. D.; Niaux, A.; Boulesbaa, A.; Neretina, S.; Borguet, E. Seeing Is Believing: Hot Electron Based Gold Nanoplasmonic Optical Hydrogen Sensor. *ACS Nano* **2014**, *8*, 7755–7762.

(14) Wang, W.; Klots, A.; Prasai, D.; Yang, Y.; Bolotin, K. I.; Valentine, J. Hot Electron-Based Near-Infrared Photodetection Using Bilayer MoS2. *Nano Lett.* **2015**, *15*, 7440–7444.

(15) Shokri Kojori, H.; Yun, J. H.; Paik, Y.; Kim, J.; Anderson, W. A.; Kim, S. J. Plasmon Field Effect Transistor for Plasmon to Electric Conversion and Amplification. *Nano Lett.* **2016**, *16*, 250–254.

(16) Linic, S.; Christopher, P.; Ingram, D. B. Plasmonic-Metal Nanostructures for Efficient Conversion of Solar to Chemical Energy. *Nat. Mater.* **2011**, *10*, 911–921.

(17) Kriegel, I.; Jiang, C.; Rodríguez-Fernández, J.; Schaller, R. D.; Talapin, D. V.; Da Como, E.; Feldmann, J. Tuning the Excitonic and Plasmonic Properties of Copper Chalcogenide Nanocrystals. *J. Am. Chem. Soc.* **2012**, *134*, 1583–1590.

(18) Pillai, S.; Green, M. a. Plasmonics for Photovoltaic Applications. *Sol. Energy Mater. Sol. Cells* **2010**, *94*, 1481–1486.

(19) Pilo-Pais, M.; Watson, a.; Demers, S.; Labean, T. H.; Finkelstein, G. Surface-Enhanced Raman Scattering Plasmonic Enhancement Using DNA Origami-Based Complex Metallic Nanostructures. *Nano Lett.* **2014**, *14*, 2099–2104.

(20) Darvill, D.; Centeno, A.; Xie, F. Plasmonic Fluorescence Enhancement by Metal Nanostructures: Shaping the Future of Bionanotechnology. *Phys. Chem. Chem. Phys.* **2013**, *15*, 15709–15726.

(21) Gao, L.; Zhang, Y.; Zhang, H.; Doshay, S.; Xie, X.; Luo, H.; Shah, D.; Shi, Y.; Xu, S.; Fang, H.; *et al.* Optics and Nonlinear Buckling Mechanics in Large-Area, Highly Stretchable Arrays of Plasmonic Nanostructures. *ACS Nano* **2015**, *9*, 5968–5975.

(22) Marinica, D. C.; Zapata, M.; Nordlander, P.; Kazansky, A. K.; M. Echenique, P.; Aizpurua, J.; Borisov, A. G. Active Quantum Plasmonics. *Sci. Adv.* **2015**, *1*, e1501095.

(23) Mendelsberg, R. J.; Garcia, G.; Li, H.; Manna, L.; Milliron, D. J. Understanding

the Plasmon Resonance in Ensembles of Degenerately Doped Semiconductor Nanocrystals. *J. Phys. Chem. C* **2012**, *116*, 12226–12231.

(24) Routzahn, A. L.; White, S. L.; Fong, L. K.; Jain, P. K. Plasmonics with Doped Quantum Dots. *Isr. J. Chem.* **2012**, *52*, 983–991.

(25) Scotognella, F.; Della Valle, G.; Srimath Kandada, A. R.; Zavelani-Rossi, M.; Longhi, S.; Lanzani, G.; Tassone, F. Plasmonics in Heavily-Doped Semiconductor Nanocrystals. *Eur. Phys. J. B* **2013**, *86*.

(26) Faucheaux, J. a.; Stanton, A. L. D.; Jain, P. K. Plasmon Resonances of Semiconductor Nanocrystals: Physical Principles and New Opportunities. *J. Phys. Chem. Lett.* **2014**, *5*, 976–985.

(27) Willets, K. a; Van Duyne, R. P. Localized Surface Plasmon Resonance Spectroscopy and Sensing. *Annu. Rev. Phys. Chem.* **2007**, *58*, 267–297.

(28) Camden, J. P.; Dieringer, J. a.; Zhao, J.; Van Duyne, R. P. Controlled Plasmonic Nanostructures for Surface-Enhanced Spectroscopy and Sensing. *Acc. Chem. Res.* **2008**, *41*, 1653–1661.

(29) Becker, J.; Trügler, A.; Jakab, A.; Hohenester, U.; Sönnichsen, C. The Optimal Aspect Ratio of Gold Nanorods for Plasmonic Bio-Sensing. *Plasmonics* **2010**, *5*, 161–167.

(30) Chen, H.; Shao, L.; Li, Q.; Wang, J. Gold Nanorods and Their Plasmonic Properties. *R. Soc. Chem.* **2015**, *42*, 2679–2724.

(31) Scholl, J. a; Koh, A. L.; Dionne, J. a. Quantum Plasmon Resonances of Individual Metallic Nanoparticles. *Nature* **2012**, *483*, 421–427.

(32) Petryayeva, E.; Krull, U. J. Localized Surface Plasmon Resonance: Nanostructures, Bioassays and Biosensing--a Review. *Anal. Chim. Acta* **2011**, *706*, 8–24.

(33) Vo-Dinh, T.; Wang, H. N.; Scaffidi, J. Plasmonic Nanoprobes for SERS Biosensing and Bioimaging. *J. Biophotonics* **2010**, *3*, 89–102.

(34) Lal, S.; Grady, N. K.; Kundu, J.; Levin, C. S.; Lassiter De, J. B.; Halas, N. J. Tailoring Plasmonic Substrates for Surface Enhanced Spectroscopies. *Chem. Soc. Rev.* **2008**, *37*, 898–911.

(35) Kundu, J.; Le, F.; Nordlander, P.; Halas, N. J. Surface Enhanced Infrared Absorption (SEIRA) Spectroscopy on Nanoshell Aggregate Substrates. **2007**.

(36) Runnerstrom, E. L.; Llordés, A.; Lounis, S. D.; Milliron, D. J. Nanostructured Electrochromic Smart Windows: Traditional Materials and NIR-Selective Plasmonic Nanocrystals. *Chem. Commun. (Camb).* **2014**, 5–7.

(37) Kriegel, I.; Rodríguez-Fernández, J.; Wisnet, A.; Zhang, H.; Waurisch, C.; Eychmüller, A.; Dubavik, A.; Govorov, A. O.; Feldmann, J. Shedding Light on Vacancy-Doped Copper Chalcogenides: Shape-Controlled Synthesis, Optical Properties, and Modeling of Copper Telluride Nanocrystals with near-Infrared Plasmon Resonances. *ACS Nano* **2013**, *7*, 4367–4377.

(38) Scotognella, F.; Della Valle, G.; Srimath Kandada, A. R.; Dorfs, D.; Zavelani-Rossi, M.; Conforti, M.; Miszta, K.; Comin, A.; Korobchevskaya, K.; Lanzani, G.; *et al.* Plasmon Dynamics in Colloidal Cu_2-xSe Nanocrystals. *Nano Lett.* **2011**, *11*, 4711–4717.

(39) Zhang, H.; Kulkarni, V.; Prodan, E.; Nordlander, P.; Govorov, A. O. Theory of Quantum Plasmon Resonances in Doped Semiconductor Nanocrystals. *J. Phys. Chem. C* **2014**, *118*.

(40) Luther, J. M.; Jain, P. K.; Ewers, T.; Alivisatos, a P. Localized Surface Plasmon Resonances Arising from Free Carriers in Doped Quantum Dots. *Nat. Mater.* **2011**, *10*, 361–366.

(41) Jain, P. K.; Manthiram, K.; Engel, J. H.; White, S. L.; Faucheaux, J. a.; Alivisatos, a. P. Doped Nanocrystals as Plasmonic Probes of Redox Chemistry. *Angew. Chemie - Int. Ed.* **2013**, *52*, 13671–13675.

(42) Rowe, D. J.; Jeong, J. S.; Mkhoyan, K. A.; Kortshagen, U. R. Phosphorus-Doped Silicon Nanocrystals Exhibiting Mid-Infrared Localized Surface Plasmon Resonance. *Nano Lett.* **2013**, *13*, 1317–1322.

(43) Benjamin L. Greenberg, Shreyashi Ganguly, Jacob T. Held, N. J. K.; K. Andre Mkhoyan, Eray S. Aydil, U. R. K. *Non-Equilibrium-Plasma-Synthesized ZnO Nanocrystals with Plasmon Resonance Tunable via Al Doping and Quantum Confinement*; 2015.

(44) Manthiram, K.; Alivisatos, a. P. Tunable Localized Surface Plasmon Resonances in Tungsten Oxide Nanocrystals. *J. Am. Chem. Soc.* **2012**, *134*, 3995–3998.

(45) Li, S. Q.; Guo, P.; Zhang, L.; Zhou, W.; Odom, T. W.; Seideman, T.; Ketterson, J. B.; Chang, R. P. H. Infrared Plasmonics with Indium–Tin-Oxide Nanorod Arrays. *ACS Nano* **2011**, *5*, 9161–9170.

(46) Hirsch, L. R.; Stafford, R. J.; Bankson, J. A.; Sershen, S. R.; Rivera, B.; Price, R. E.; Hazle, J. D.; Halas, N. J.; West, J. L. Nanoshell-Mediated near-Infrared Thermal Therapy of Tumors under Magnetic Resonance Guidance. *Proc. Natl. Acad. Sci. U. S. A.* **2003**, *100*, 13549–13554.

(47) Jain, P. K.; Huang, X.; El-Sayed, I. H.; El-Sayed, M. A. Review of Some Interesting Surface Plasmon Resonance-Enhanced Properties of Noble Metal Nanoparticles and Their Applications to Biosystems. *Plasmonics* **2007**, *2*, 107–118.

(48) Dreaden, E. C.; Alkilany, A. M.; Huang, X.; Murphy, C. J.; El-Sayed, M. A. The Golden Age: Gold Nanoparticles for Biomedicine. *Chem. Soc. Rev.* **2012**, *41*, 2740–2779.

(49) Pillai, S.; Catchpole, K. R.; Trupke, T.; Green, M. A. Surface Plasmon Enhanced Silicon Solar Cells. *J. Appl. Phys.* **2007**, *101*, 93105.

(50) Ozbay, E. Plasmonics: Merging Photonics and Electronics at Nanoscale Dimensions. *Science (80-.).* **2006**, *311*, 189–193.

(51) Clavero, C. Plasmon-Induced Hot-Electron Generation at Nanoparticle/metal-Oxide Interfaces for Photovoltaic and Photocatalytic Devices. *Nat. Photonics* **2014**, *8*, 95–103.

(52) Llordes, A.; Garcia, G.; Gazquez, J.; Milliron, D. J. nature12398. *Nature* **2013**, *500*, 323–326.

(53) Wang, F.; Melosh, N. a. Plasmonic Energy Collection through Hot Carrier Extraction. *Nano Lett.* **2011**, *11*, 5426–5430.

(54) Cushing, S. K.; Li, J.; Meng, F.; Senty, T. R.; Suri, S.; Zhi, M.; Li, M.; Bristow, A. D.; Wu, N. Photocatalytic Activity Enhanced by Plasmonic Resonant Energy Transfer from Metal to Semiconductor. *J. Am. Chem. Soc.* **2012**, *134*, 15033–15041.

(55) Atwater, H. a; Polman, A. Plasmonics for Improved Photovoltaic Devices. *Nat. Mater.* **2010**, *9*, 205–213.

(56) McFarland, E. W.; Tang, J. A Photovoltaic Device Structure Based on Internal Electron Emission. *Nature* **2003**, *421*, 616–618.

(57) Govorov, A. O.; Zhang, H.; Demir, H. V.; Gun'ko, Y. K. Photogeneration of Hot Plasmonic Electrons with Metal Nanocrystals: Quantum Description and Potential Applications. *Nano Today* **2014**, *9*, 85–101.

(58) Brongersma, M. L.; Halas, N. J.; Nordlander, P. Plasmon-Induced Hot Carrier Science and Technology. *Nat. Nanotechnol.* **2015**, *10*.

(59) Liu, X.; Swihart, M. T. Heavily-Doped Colloidal Semiconductor and Metal Oxide Nanocrystals: An Emerging New Class of Plasmonic Nanomaterials. *Chem. Soc. Rev.* **2014**, *43*, 3908–3920.

(60) Vollmer, M.; Kreibig, U. *Optical Properties of Metal Clusters*; Springer Ser. Mat. Sci, 1995.

(61) Kanehara, M.; Koike, H.; Yoshinaga, T.; Teranishi, T. Indium Tin Oxide Nanoparticles with Compositionally Tunable Surface Plasmon Resonance Frequencies in the Near-IR Region. *J. Am. Chem. Soc.* **2009**, *131*, 17736–17737.

(62) Buonsanti, R.; Llordes, A.; Aloni, S.; Helms, B. A.; Milliron, D. J. Tunable Infrared Absorption and Visible Transparency of Colloidal Aluminum-Doped Zinc Oxide Nanocrystals. *Nano Lett.* **2011**, *11*, 4706–4710.

(63) Zhou, S.; Pi, X.; Ni, Z.; Ding, Y.; Jiang, Y.; Jin, C.; Delerue, C. Comparative Study on the Localized Surface Plasmon Resonance Silicon Nanocrystals. *ACS Nano* **2015**, *9*, 378–386.

(64) Dorfs, D.; Härtling, T.; Miszta, K.; Bigall, N. C.; Kim, M. R.; Genovese, A.; Falqui, A.; Povia, M.; Manna, L. Reversible Tunability of the Near-Infrared Valence Band Plasmon Resonance in Cu 2{\textendash} xSe Nanocrystals. *J. Am. Chem. Soc.* **2011**, *133*, 11175–11180.

(65) Liu, L.; Zhong, H.; Bai, Z.; Zhang, T.; Fu, W.; Shi, L.; Xie, H.; Deng, L.; Zou, B. Controllable Transformation from Rhombohedral Cu 1.8S Nanocrystals to Hexagonal CuS Clusters: Phase- and Composition-Dependent Plasmonic Properties. *Chem. Mater.* **2013**, *25*, 4828–4834.

(66) Wheeler, L. M.; Neale, N. R.; Chen, T.; Kortshagen, U. R. Hypervalent Surface Interactions for Colloidal Stability and Doping of Silicon Nanocrystals. *Nat. Commun.* **2013**, *4*.

(67) Kriegel, I.; Jiang, C.; Rodr'\iguez-Fernández, J.; Schaller, R. D.; Talapin, D. V; da Como, E.; Feldmann, J. Tuning the Excitonic and Plasmonic Properties of Copper Chalcogenide Nanocrystals. *J. Am. Chem. Soc.* **2012**, *134*, 1583–1590.

(68) Thimsen, E.; Johnson, M.; Zhang, X.; Wagner, A. J.; Mkhoyan, K. A.; Kortshagen, U. R.; Aydil, E. S. High Electron Mobility in Thin Films Formed via Supersonic Impact Deposition of Nanocrystals Synthesized in Nonthermal

Plasmas. *Nat. Commun.* **2014**, *5*, 5822.

(69) Stanley, R. Plasmonics in the Mid-Infrared. *Nat. Photonics* **2012**, *6*, 409–411.

(70) Law, S.; Podolskiy, V.; Wasserman, D. Towards Nano-Scale Photonics with Micro-Scale Photons: The Opportunities and Challenges of Mid-Infrared Plasmonics. *Nanophotonics* **2015**, *2*, 1–29.

(71) Gresback, R.; Kramer, N. J.; Ding, Y.; Chen, T.; Kortshagen, U. R.; Nozaki, T. Controlled Doping of Silicon Nanocrystals Investigated by Solution-Processed Field Effect Transistors. *ACS Nano* **2014**, *8*.

(72) Chen, X.; Pi, X.; Yang, D. Critical Role of Dopant Location for P-Doped Si Nanocrystals. *J. Phys. Chem. C* **2010**, *115*, 661–666.

(73) Ong, C. W.; Chik, K. P.; Wong, H. K. Properties of a-Boron Films Prepared by Low Pressure Chemical Vapour Deposition. *J. Non-Cryst. Solids* **1989**, *114*, 783–785.

(74) Saß, M.; Annen, A.; Jacob, W. Hydrogen Bonding in Plasma-Deposited Amorphous Hydrogenated Boron Films. *J. Appl. Phys.* **1997**, *82*, 1905–1908.

(75) Ma, J.; Wei, S. H.; Neale, N. R.; Nozik, A. J. Effect of Surface Passivation on Dopant Distribution in Si Quantum Dots: The Case of B and P Doping. *Appl. Phys. Lett.* **2011**, *98*, 173103.

(76) Ma, J.; Wei, S. H. Chemical Trend of the Formation Energies of the Group-III and Group-V Dopants in Si Quantum Dots. *Phys. Rev. B* **2013**, *87*, 115318.

(77) Guerra, R.; Ossicini, S. Preferential Positioning of Dopants and Co-Dopants in Embedded and Freestanding Si Nanocrystals. *J. Am. Chem. Soc.* **2014**, *136*, 4404–4409.

(78) Pi, X.; Chen, X.; Yang, D. First-Principles Study of 2.2 Nm Silicon Nanocrystals Doped with Boron. *J. Phys. Chem. C* **2011**, *115*, 9838–9843.

(79) Cabrera, N.; Mott, N. F. Theory of the Oxidation of Metals. *Reports Prog. Phys.* **1949**, *12*, 163–184.

(80) Niesar, S.; Stegner, A. R.; Pereira, R. N.; Hoeb, M.; Wiggers, H.; Brandt, M. S.; Stutzmann, M. Defect Reduction in Silicon Nanoparticles by Low-Temperature Vacuum Annealing. *Appl. Phys. Lett.* **2010**, *96*, 193112.

(81) Pereira, R. N.; Rowe, D. J.; Anthony, R. J.; Kortshagen, U. Oxidation of

Freestanding Silicon Nanocrystals Probed with Electron Spin Resonance of Interfacial Dangling Bonds. *Phys. Rev. B - Condens. Matter Mater. Phys.* **2011**, *83*, 1–9.

(82) Quirt, J.; Marko, J. Absolute Spin Susceptibilities and Other ESR Parameters of Heavily Doped N-Type Silicon. I. Metallic Samples. *Phys. Rev. B* **1972**, *5*, 1716–1728.

(83) Sumida, K.; Ninomiya, K.; Fujii, M.; Fujio, K.; Hayashi, S.; Kodama, M.; Ohta, H. Electron Spin-Resonance Studies of Conduction Electrons in Phosphorus-Doped Silicon Nanocrystals. *J. Appl. Phys.* **2007**, *101*, 33504.

(84) Fujio, K.; Fujii, M.; Sumida, K.; Hayashi, S.; Fujisawa, M.; Ohta, H. Electron Spin Resonance Studies of P and B Codoped Si Nanocrystals. *Appl. Phys. Lett.* **2008**, *93*, 21920.

(85) Stegner, A.; Pereira, R.; Klein, K.; Lechner, R.; Dietmueller, R.; Brandt, M.; Stutzmann, M.; Wiggers, H. Electronic Transport in Phosphorus-Doped Silicon Nanocrystal Networks. *Phys. Rev. Lett.* **2008**, *100*, 26803.

(86) Zhou, S.; Ding, Y.; Pi, X.; Nozaki, T. Doped Silicon Nanocrystals from Organic Dopant Precursor by a SiCl4-Based High Frequency Nonthermal Plasma. *Appl. Phys. Lett.* **2014**, *105*, 183110.

(87) Puthen Veettil, B.; Wu, L.; Jia, X.; Lin, Z.; Zhang, T.; Yang, T.; Johnson, C.; McCamey, D.; Conibeer, G.; Perez-Würfl, I. Passivation Effects in B Doped Self-Assembled Si Nanocrystals. *Appl. Phys. Lett.* **2014**, *105*, 222108.

(88) Perego, M.; Bonafos, C.; Fanciulli, M. Phosphorus Doping of Ultra-Small Silicon Nanocrystals. *Nanotechnology* **2009**, *21*, 25602.

(89) Kazahaya, T.; Hirose, M. Coordination-Number of Doped Boron Atoms in Photochemically-Deposited Amorphous-Silicon Studied by X-Ray Photoelectron-Spectroscopy. *Jpn. J. Appl. Phys.* **1986**, *25*, L75--L77.

(90) Tsutsui, K.; Matsuda, T.; Watanabe, M.; Jin, C.-G.; Sasaki, Y.; Mizuno, B.; Ikenaga, E.; Kakushima, K.; Ahmet, A.; Maruizumi, T.; *et al.* Activated Boron and Its Concentration Profiles in Heavily Doped Si Studied by Soft X-Ray Photoelectron Spectroscopy and Hall Measurements. *J. Appl. Phys.* **2008**, *104*, 93709.

(91) Yamauchi, J.; Yoshimoto, Y.; Suwa, Y. Identification of Boron Clusters in Silicon Crystal by B1s Core-Level X-Ray Photoelectron Spectroscopy: A First-Principles Study. *Appl. Phys. Lett.* **2011**, *99*, 191901.

(92) Ristein, J. Surface Transfer Doping of Semiconductors. *Science (80-.).* **2006**, *313*, 1057–1058.

(93) Chen, W.; Qi, D.; Gao, X.; Wee, A. T. S. Surface Transfer Doping of Semiconductors. *Prog. Surf. Sci.* **2009**, *84*, 279–321.

(94) Nguyen, M. T.; Matus, M. H.; Ngan, V. T.; Grant, D. J.; Dixon, D. A. Thermochemistry and Electronic Structure of Small Boron and Boron Oxide Clusters and Their Anions. *J. Phys. Chem. A* **2009**, *113*, 4895–4909.

(95) Madelung, O. *Semiconductors: Data Handbook*; Springer Science & Business Media, 2012.

(96) Billinge, S. J. L.; Kanatzidis, M. G. Beyond Crystallography: The Study of Disorder, Nanocrystallinity and Crystallographically Challenged Materials with Pair Distribution Functions. *Chem. Commun.* **2004**, 749.

(97) Petkov, V. Nanostructure by High-Energy X-Ray Diffraction. *Mater. Today* **2008**, *11*, 28–38.

(98) Bedford, N. M.; Ramezani-Dakhel, H.; Slocik, J. M.; Briggs, B. D.; Ren, Y.; Frenkel, A. I.; Petkov, V.; Heinz, H.; Naik, R. R.; Knecht, M. R. Elucidation of Peptide-Directed Palladium Surface Structure for Biologically Tunable Nanocatalysts. *ACS Nano* **2015**, *9*, 5082–5092.

(99) Petkov, V.; Hessel, C. M.; Ovtchinnikoff, J.; Guillaussier, A.; Korgel, B. A.; Liu, X.; Giordano, C. Structure-Properties Correlation in Si Nanoparticles by Total Scattering and Computer Simulations. *Chem. Mater.* **2013**, *25*, 2365–2371.

(100) Keen, D. A.; McGreevy, R. L. Structural Modelling of Glasses Using Reverse Monte Carlo Simulation. *Nature*, 1990, *344*, 423–425.

(101) Le Roux, S.; Martin, S.; Christensen, R.; Ren, Y.; Petkov, V. Three-Dimensional Structure of Multicomponent (Na2O)(0.35)[(P2O5)(1-x)(B2O3)(x)](0.65) Glasses by High-Energy X-Ray Diffraction and Constrained Reverse Monte Carlo Simulations. *J. Physics-Condensed Matter* **2011**, *23*.

(102) Bedford, N.; Dablemont, C.; Viau, G.; Chupas, P.; Petkov, V. 3-D Structure of Nanosized Catalysts by High-Energy X-Ray Diffraction and Reverse Monte Carlo Simulations: Study of Ru. *J. Phys. Chem. C* **2007**, *111*, 18214–18219.

(103) Petkov, V. RAD, a Program for Analysis of X-Ray Diffraction Data from Amorphous Materials for Personal Computers. *J. Appl. Crystallogr.* **1989**, *22*,

387–389.

(104) Gereben, O.; Petkov, V. Reverse Monte Carlo Study of Spherical Sample under Non-Periodic Boundary Conditions: The Structure of Ru Nanoparticles Based on X-Ray Diffraction Data. *J Phys Condens Matter* **2013**, *25*, 454211.

(105) Bapat, A.; Anderson, C.; Perrey, C. R.; Carter, C. B.; Campbell, S. A.; Kortshagen, U. Plasma Synthesis of Single-Crystal Silicon Nanoparticles for Novel Electronic Device Applications. *Plasma Phys. Control. Fusion* **2004**, *46*, B97–B109.

(106) Klein, D. L.; Roth, R.; Lim, A. K. L.; Alivisatos, A. P.; Mceuen, P. L. A Single-Electron Transistor Made from a Cadmium Selenide Nanocrystal. *Nature* **1997**, *389*.

(107) Wagner, A. J.; Hintsala, E. D.; Kumar, P.; Gerberich, W. W.; Mkhoyan, K. A. Mechanisms of Plasticity in near-Theoretical Strength Sub-100 Nm Si Nanocubes. *Acta Mater.* **2015**, *100*, 256–265.

(108) Burda, C.; Chen, X.; Narayanan, R.; El-Sayed, M. A. Chemistry and Properties of Nanocrystals of Different Shapes. *Chem. Rev.* **2005**, *105*, 1025–1102.

(109) Eustis, S.; El-Sayed, M. A. Why Gold Nanoparticles Are More Precious than Pretty Gold: Noble Metal Surface Plasmon Resonance and Its Enhancement of the Radiative and Nonradiative Properties of Nanocrystals of Different Shapes. *Chem. Soc. Rev.* **2005**, *35*, 209–217.

(110) Roduner, E. Size Matters: Why Nanomaterials Are Different. *Chem. Soc. Rev.* **2006**, *35*, 583–592.

(111) Cui, Y.; Zhong, Z.; Wang, D.; Wang, W. U.; Lieber, C. M. High Performance Silicon Nanowire Field Effect Transistors. *Nano Lett.* **2003**, *3*, 149–152.

(112) Fuechsle, M.; Mahapatra, S.; Zwanenburg, F. A.; Friesen, M.; Eriksson, M. A.; Simmons, M. Y. Spectroscopy of Few-Electron Single-Crystal Silicon Quantum Dots. *Nat. Nanotechnol.* **2010**, *5*, 502–505.

(113) Pereira, R. N.; Rowe, D. J.; Anthony, R. J.; Kortshagen, U. Freestanding Silicon Nanocrystals with Extremely Low Defect Content. *Phys. Rev. B - Condens. Matter Mater. Phys.* **2012**, *86*, 1–6.

(114) Mangolini, L.; Jurbergs, D.; Rogojina, E.; Kortshagen, U. Plasma Synthesis and Liquid-Phase Surface Passivation of Brightly Luminescent Si Nanocrystals. *J. Lumin.* **2006**, *121*, 327–334.

(115) Dickerson, E. B.; Dreaden, E. C.; Huang, X.; El-Sayed, I. H.; Chu, H.; Pushpanketh, S.; McDonald, J. F.; El-Sayed, M. a. Gold Nanorod Assisted near-Infrared Plasmonic Photothermal Therapy (PPTT) of Squamous Cell Carcinoma in Mice. *Cancer Lett.* **2008**, *269*, 57–66.

(116) Li, J.; Guo, H.; Li, Z. Microscopic and Macroscopic Manipulation of Gold Nanorod and Its Hybrid Nanostructures [Invited]. *Photonics Res.* **2013**, *1*, 28–41.

(117) Yang, J.; Kramer, N. J. N. J.; Schramke, K. S. K. S.; Wheeler, L. M. L. M.; Besteiro, L. V. L. V.; Hogan, C. J. C. J.; Govorov, A. O. A. O.; Kortshagen, U. R. U. R. Broadband Absorbing Exciton-Plasmon Metafluids with Narrow Transparency Windows. *Nano Lett.* **2016**, *16*, 1472–1477.

(118) Nik, B.; Sayed, a El. Preparation and Growth Mechanism of Gold Nanorods (NRs) Using Seed - Mediated Growth Method. *Chem. Mater.* **2003**, *15*, 1957–1962.

(119) Xu, L.; Kuang, H.; Wang, L.; Xu, C. Gold Nanorod Ensembles as Artificial Molecules for Applications in Sensors. *J. Ma* **2011**, *21*, 16759–16782.

(120) Khatua, S.; Paulo, P. M. R.; Yuan, H.; Gupta, A.; Zijlstra, P.; Orrit, M. Resonant Plasmonic Enhancement of Single-Molecule Fluorescence by Individual Gold Nanorods. *ACS Nano* **2014**, *8*, 4440–4449.

(121) Kortshagen, U. R.; Sankaran, R. M.; Pereira, R. N.; Girshick, S. L.; Wu, J. J.; Aydil, E. S. Nonthermal Plasma Synthesis of Nanocrystals: Fundamental Principles, Materials, and Applications. *Chemical Reviews*, 2016, *116*.

(122) Guler, U.; Naik, G.; Boltasseva, A.; Shalaev, V.; Kildishev, A. Nitrides as Alternative Materials for Localized Surface Plasmon Applications. *Front. Opt. 2012/Laser Sci. XXVIII* **2012**, *1*, FTh4A.2.

(123) Gururaj, V. N.; Schroeder, J. L.; Ni, X.; Kildishev, A.; Sands, T.; Boltasseva, A. Titanium Nitride as a Plasmonic Material for Visible and near-Infrared Wavelengths. *Opt. Mater. Express* **2012**, *2*, 478–489.

(124) Alvarez Barragan, A.; Ilawe, N. V.; Zhong, L.; Wong, B. M.; Mangolini, L. A Non-Thermal Plasma Route to Plasmonic TiN Nanoparticles. *J. Phys. Chem. C* **2017**, *121*, 2316–2322.

(125) Cortie, M. B.; Giddings, J.; Dowd, a. Optical Properties and Plasmon Resonances of Titanium Nitride Nanostructures. *Nanotechnology* **2010**, *21*, 115201.

(126) Miller, P. J.; Colson, S. D.; Chupka, W. A. Observation of the ν1+nν2

Combination Band in the C̃′ 1A1′ Rydberg State of NH3. *Chem. Phys. Lett.* **1988**, *145*, 183–187.

(127) Afanasyev-Charkin, I. V.; Nastasi, M. Hard Si–N–C Coatings Produced by Pulsed Glow Discharge Deposition. *Surf. Coat. Technol.* **2004**, *186*, 108–111.

(128) Dubois, L. H.; Zegarski, B. R. Infrared Studies of the Surface and Gas Phase Reactions Leading to the Growth of Titanium Nitride Thin Films from Tetrakis(dimethylamido)titanium and Ammonia. *J. Electrochem. Soc.* **1992**, *139*, 3603–3609.

(129) Huang, S.; Tour, J. M. Rapid Solid-Phase Synthesis of oligo(1,4-Phenylene Ethynylene)s by a Divergent/convergent Tripling Strategy. *J. Am. Chem. Soc.* **1999**, *121*, 4908.

(130) Oliveira, C.; Gonçalves, L.; Almeida, B. G.; Tavares, C. J.; Carvalho, S.; Vaz, F.; Escobar_Galindo, R.; Henriques, M.; Susano, M.; Oliveira, R. XRD and FTIR Analysis of Ti–Si–C–ON Coatings for Biomedical Applications. *Surf. Coat. Technol.* **2008**, *203*, 490–494.

(131) Musher, J. N.; Gordon, R. G. Atmospheric Pressure Chemical Vapor Deposition of TiN from Tetrakis(dimethylamido)titanium and Ammonia. *J. Mater. Res.* **1996**, *11*, 989–1001.

(132) Gordon, R. G.; Frisbie, R. W.; Musher, J.; Thornton, J. Atmospheric Pressure Chemical Vapor Deposition of Titanium Nitride from Titanium Bromide And Ammonia. *MRS Proc.* **1995**, *410*, 736–744.

(133) Lee, Y. J. Low-Impurity, Highly Conformal Atomic Layer Deposition of Titanium Nitride Using NH3-Ar-H2 Plasma Treatment for Capacitor Electrodes. *Mater. Lett.* **2005**, *59*, 615–617.

(134) Yun, J.-Y. Comparison of Tetrakis(dimethylamido)titanium and Tetrakis(diethylamido)titanium as Precursors for Metallorganic Chemical Vapor Deposition of Titanium Nitride. *J. Electrochem. Soc.* **1999**, *146*, 1804.

(135) Musschoot, J.; Xie, Q.; Deduytsche, D.; Van den Berghe, S.; Van Meirhaeghe, R. L.; Detavernier, C. Atomic Layer Deposition of Titanium Nitride from TDMAT Precursor. *Microelectron. Eng.* **2009**, *86*, 72–77.

7. Appendices

7.1. Supporting Information from Chapter 2

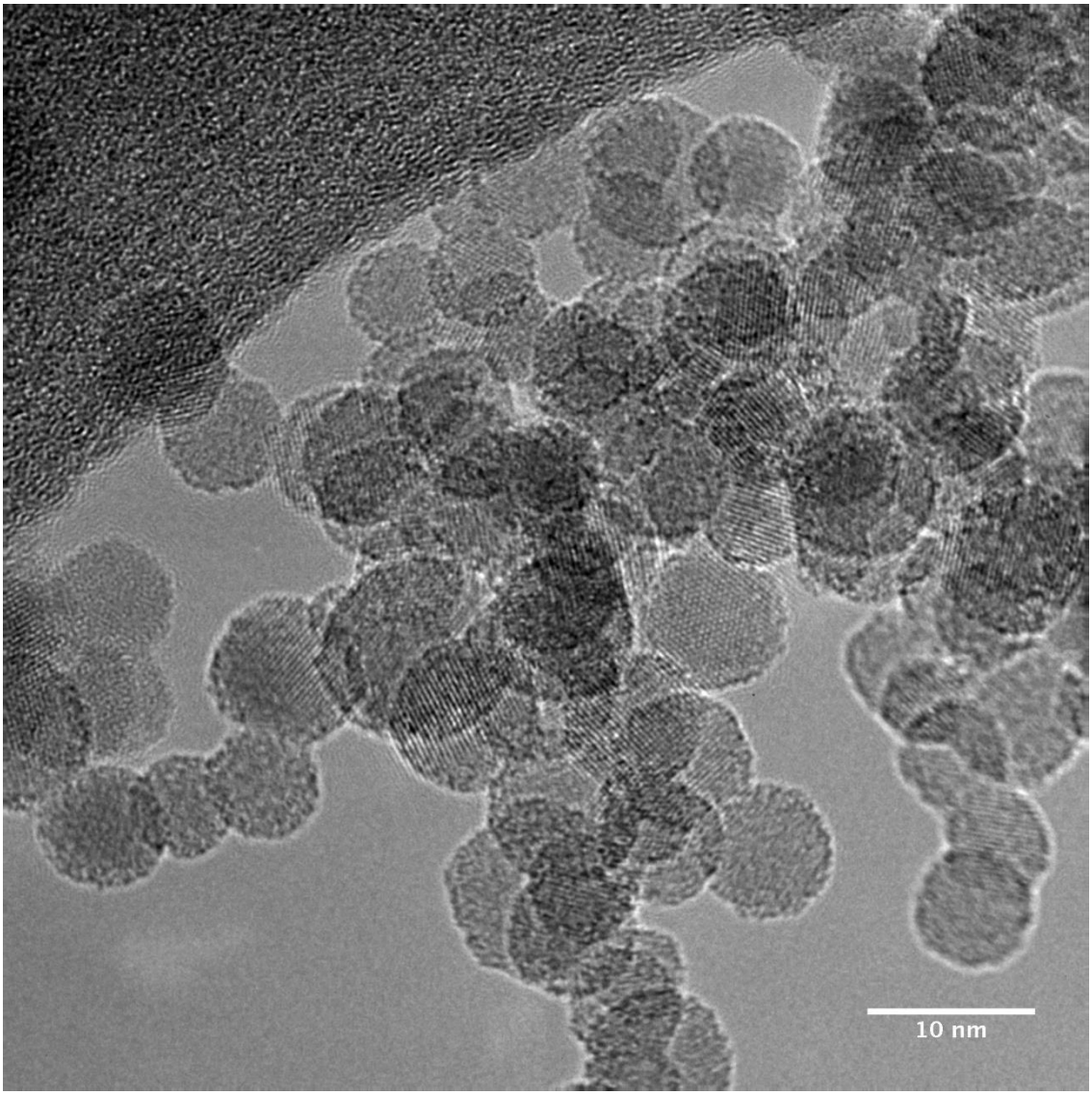

***Figure 7.1.1**:* Transmission Electron Microscope image of the 8 nm silicon nanocrystals that were used in this study.

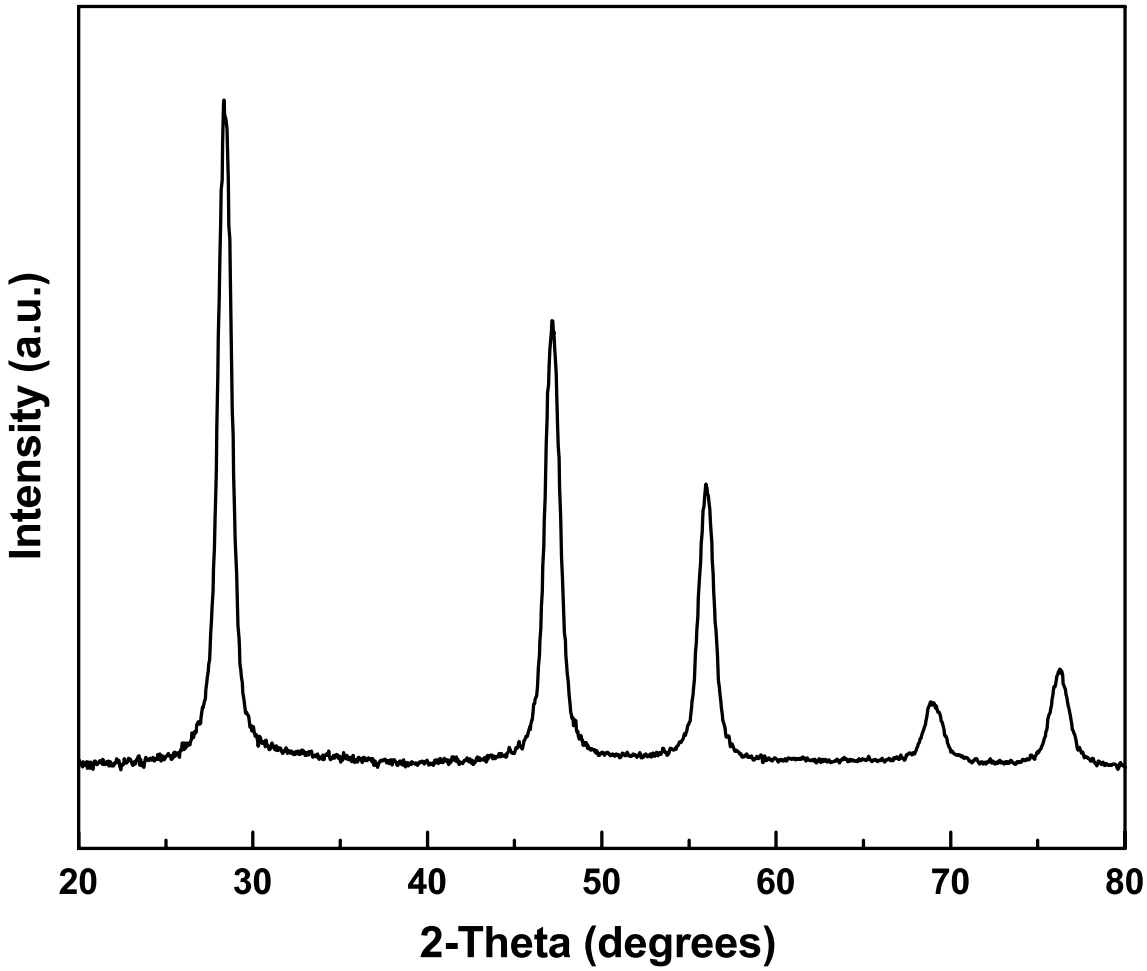

Figure 7.1.2: X-Ray Diffraction spectrum of silicon nanocrystals. The Scherrer equation gives an average size of 8.3 nm, which agrees well with the TEM results.

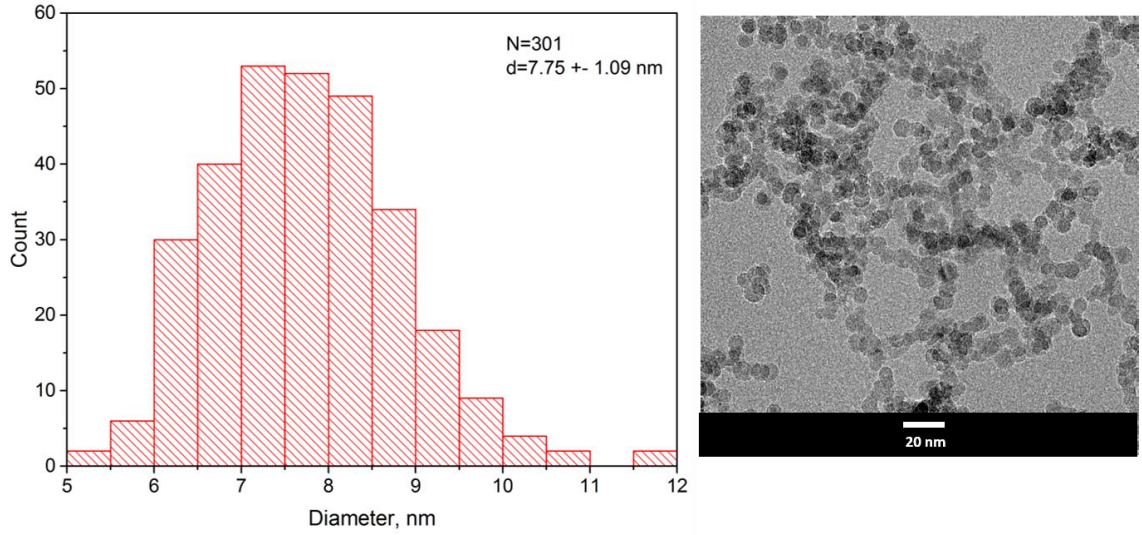

Figure 7.1.3: Size distribution of nanocrystals and one of the TEM images used to analyze the size distribution.

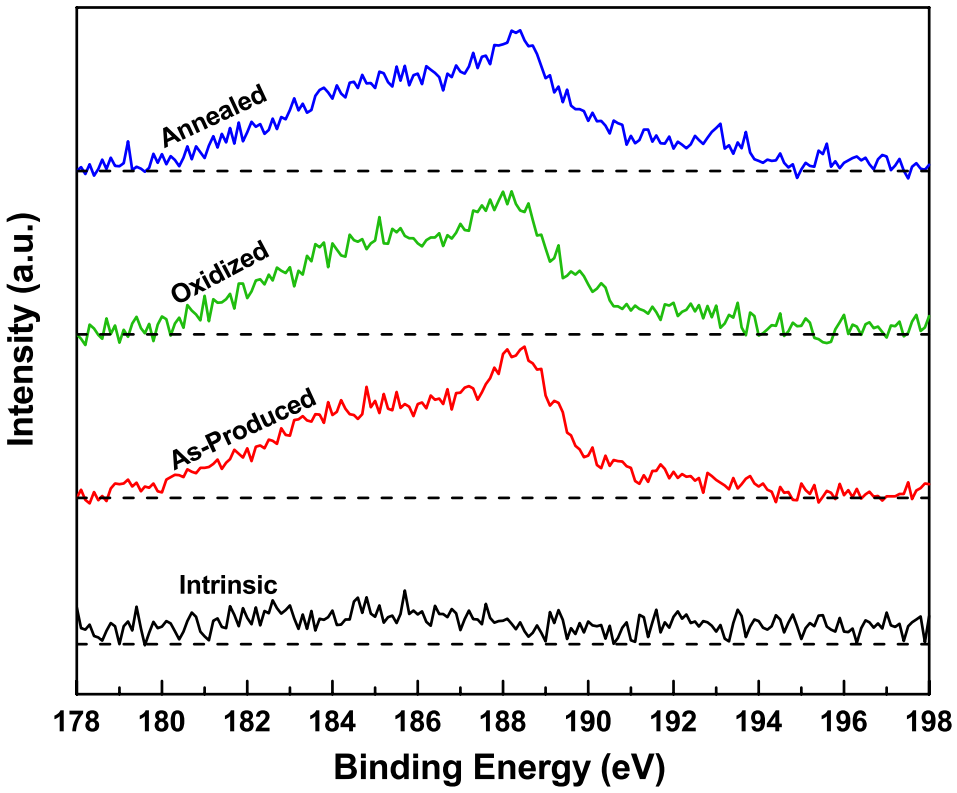

Figure 7.1.4: X-Ray Photoelectron Spectroscopy results for intrinsic (black) and B-doped (red, green and blue) silicon nanocrystals. The spectra show the difference in the trivalent and tetravalent states of boron for as-produced and post-synthesis treated nanocrystals.

.

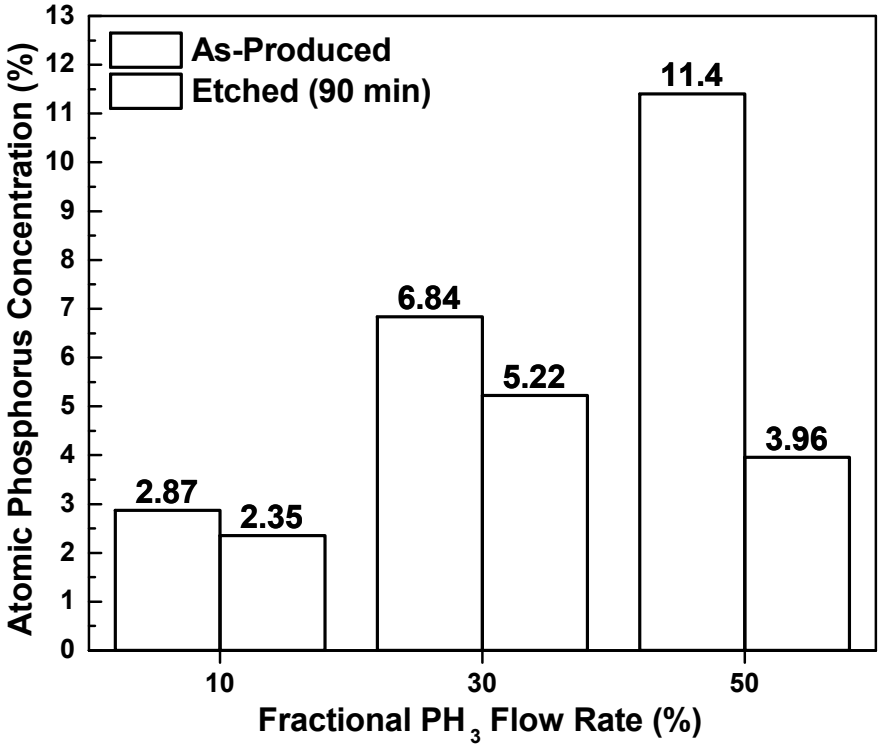

Figure 7.1.5: Atomic phosphorus concentration for as-produced and HF etched P-doped silicon nanocrystals obtained via Energy-dispersive X-Ray Spectroscopy.

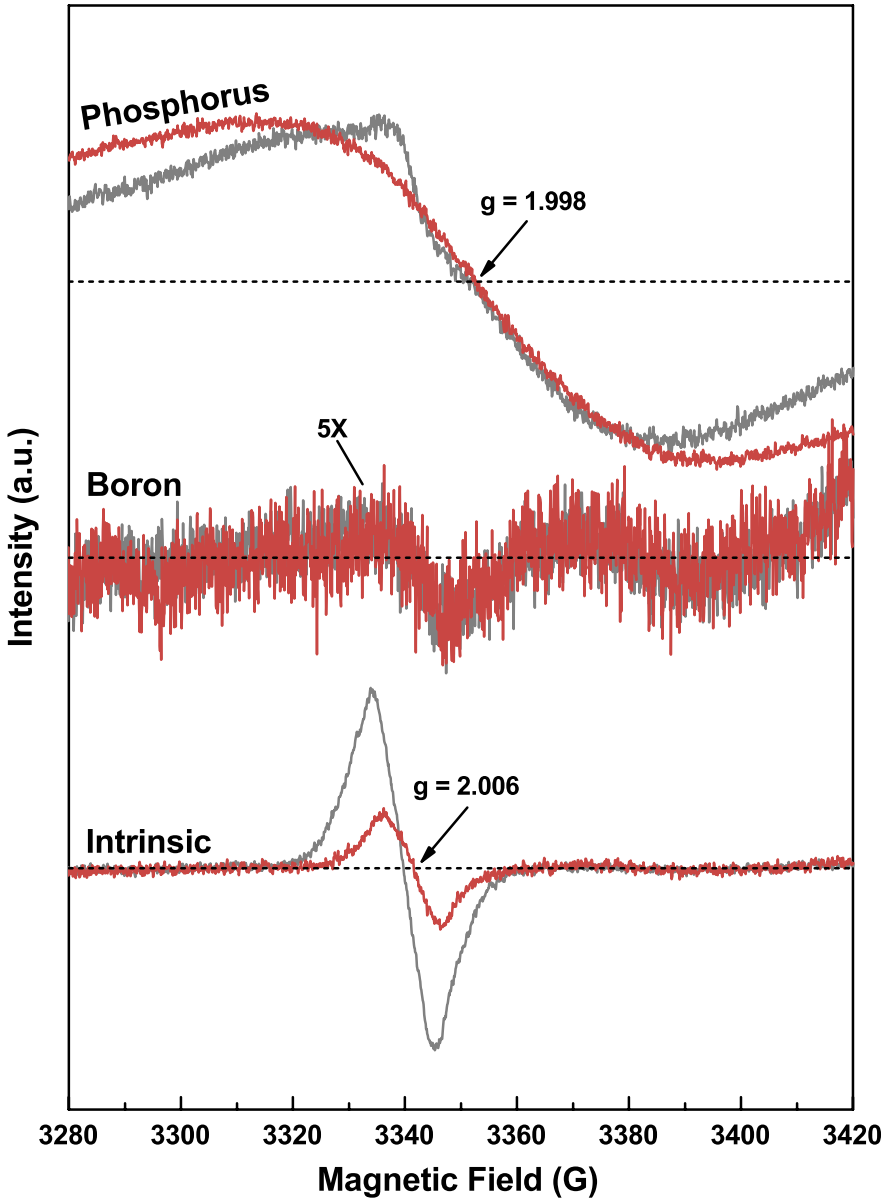

Figure 7.1.6: Electron Paramagnetic Resonance (EPR) spectra for as-produced (gray) and annealed (red) Si NCs. A reduction in signal is observed for annealed intrinsic NCs as a result of surface restructuring and defect reduction. A feature is also removed from the P-doped spectrum, likely caused by a similar reduction in defects. The B-doped spectrum does not change significantly after annealing.

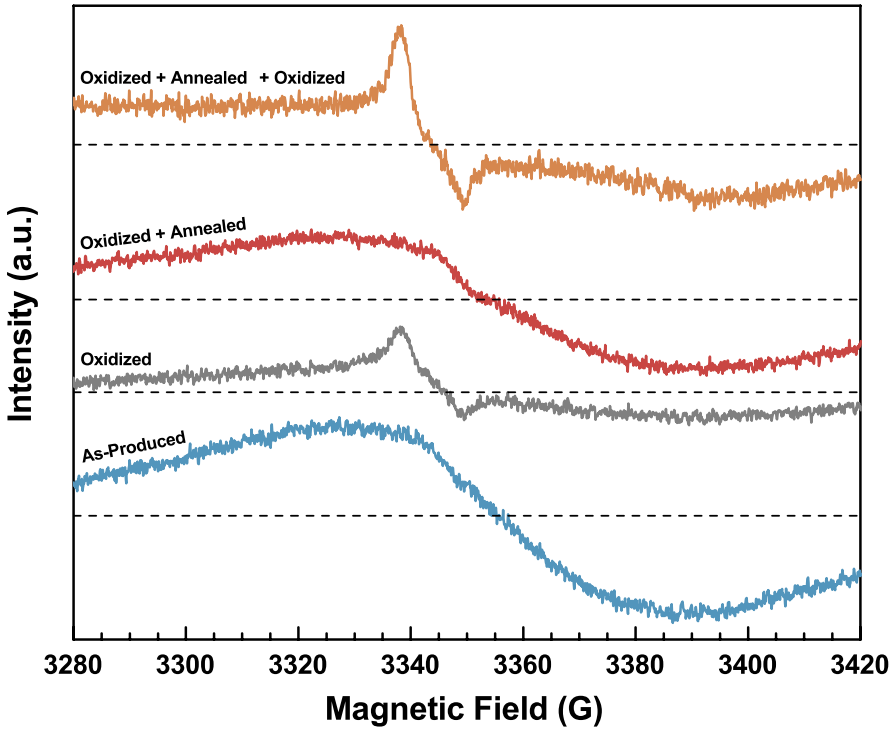

Figure 7.1.7: Electron Paramagnetic Resonance (EPR) spectra for as-produced and post-synthesis treated P-doped Si NCs. As-produced (blue) NCs exhibit a broad absorption as a result of free conduction electrons. After oxidation (gray) the spectrum changes due to the formation of an oxide shell, giving rise to P_b defects. A subsequent annealing treatment (red) reduces the number of defects and a broad absorption returns which resembles the spectrum of as-produced NCs. This can be reversed again by re-oxidation (orange) of the NCs.

To determine the influence of the dopant distribution on the absorption, absorption spectra is calculated for different doping cases:

Doping Case	Dopant Distribution
Bulk	$\rho(r) = n_0$, where n_0 is a constant
Surface	$\rho(r) = \sigma\delta(r - R)$, where σ is a constant
Exponential	$\rho(r) = \exp(\alpha r) - 1$, α is a constant, $r<R$

We employ the one-component theory, where only the heavy component is considered. The diameter of the nanoparticle is 8 nm and the number of dopants within the particle is fixed at N=268. The carrier distribution for different doping cases and the corresponding absorption spectra are given in Figure *7.1.8*.

Although the carrier distributions show significant differences among the three doping cases, the general profiles of the absorption spectra are similar. Within the one-component theory, different carrier distributions will only induce small shifts in peak plasmon resonance energies.

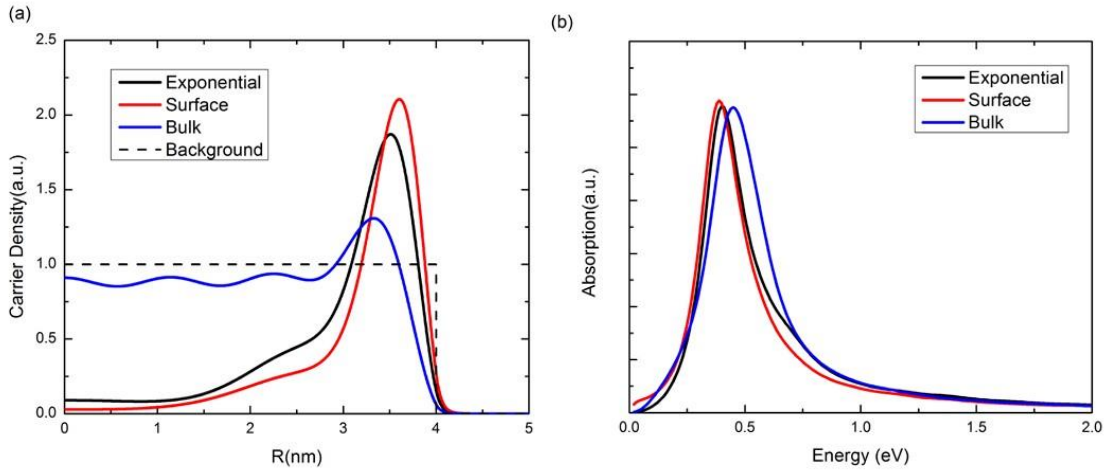

Figure 7.1.8: (a) The free carrier densities of different doping cases. (b) Corresponding absorption spectra of different doping cases.

7.2. Supporting Information from Chapter 4

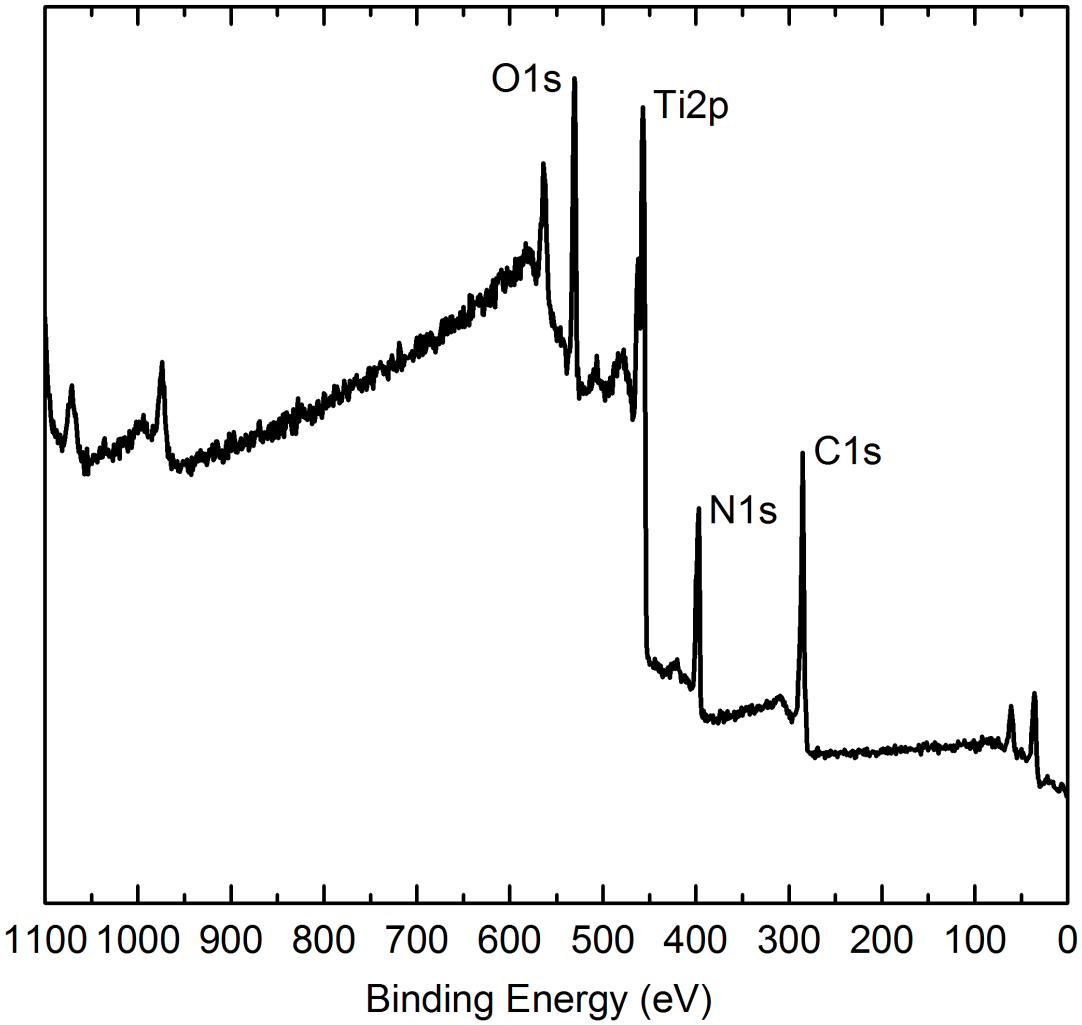

Figure 7.2.1: XPS survey scan of TiN NCs.

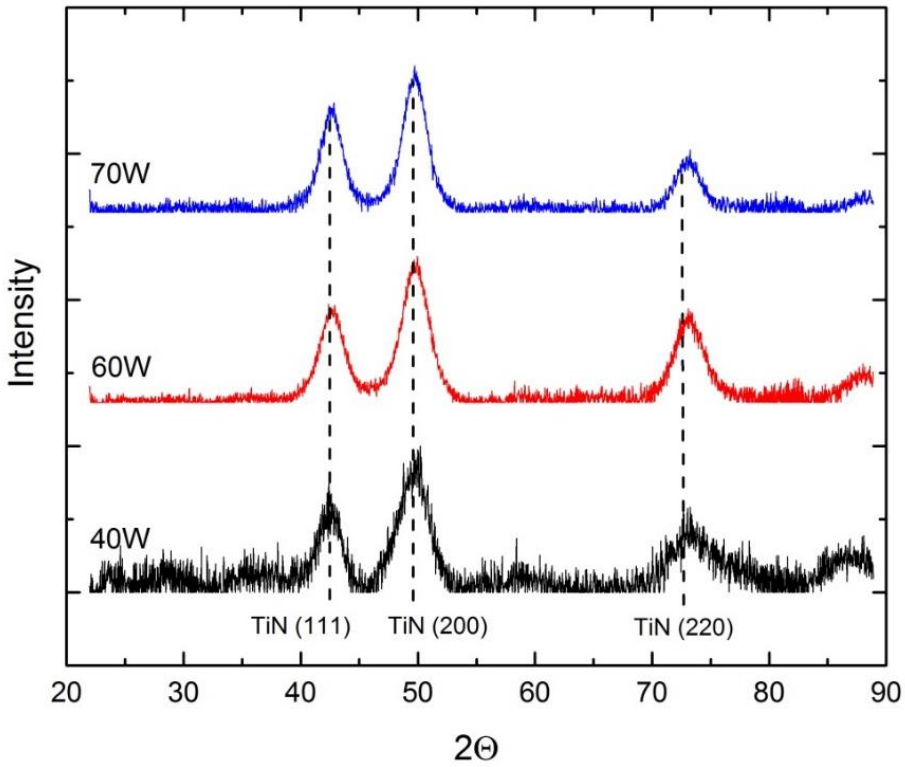

Figure 7.2.2: XRD patterns of TiN for increasing nominal power. The peaks are labeled with corresponding TiN crystal planes.

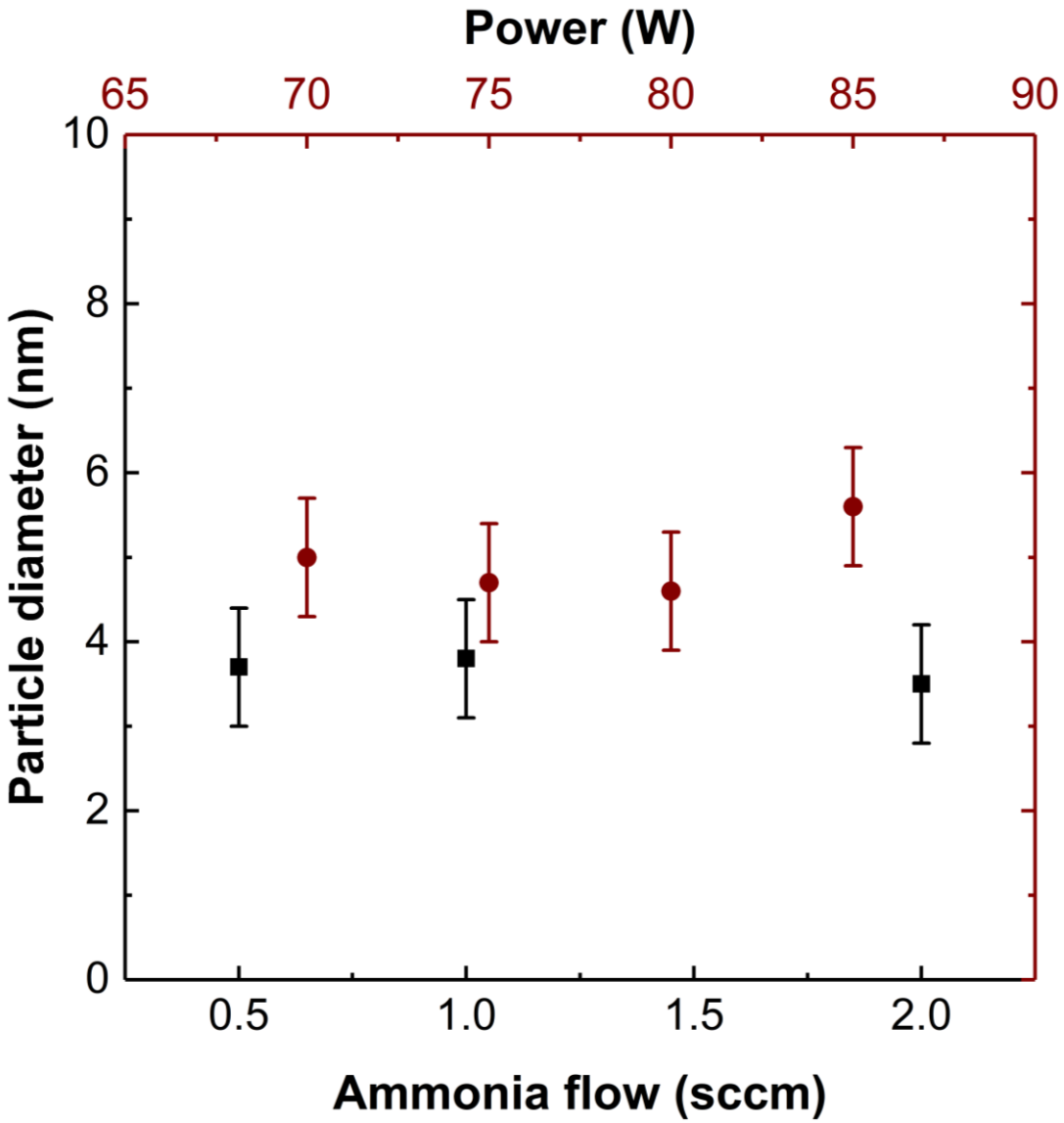

Figure 7.2.3: Particle size dependence on ammonia flow and nominal synthesis power.

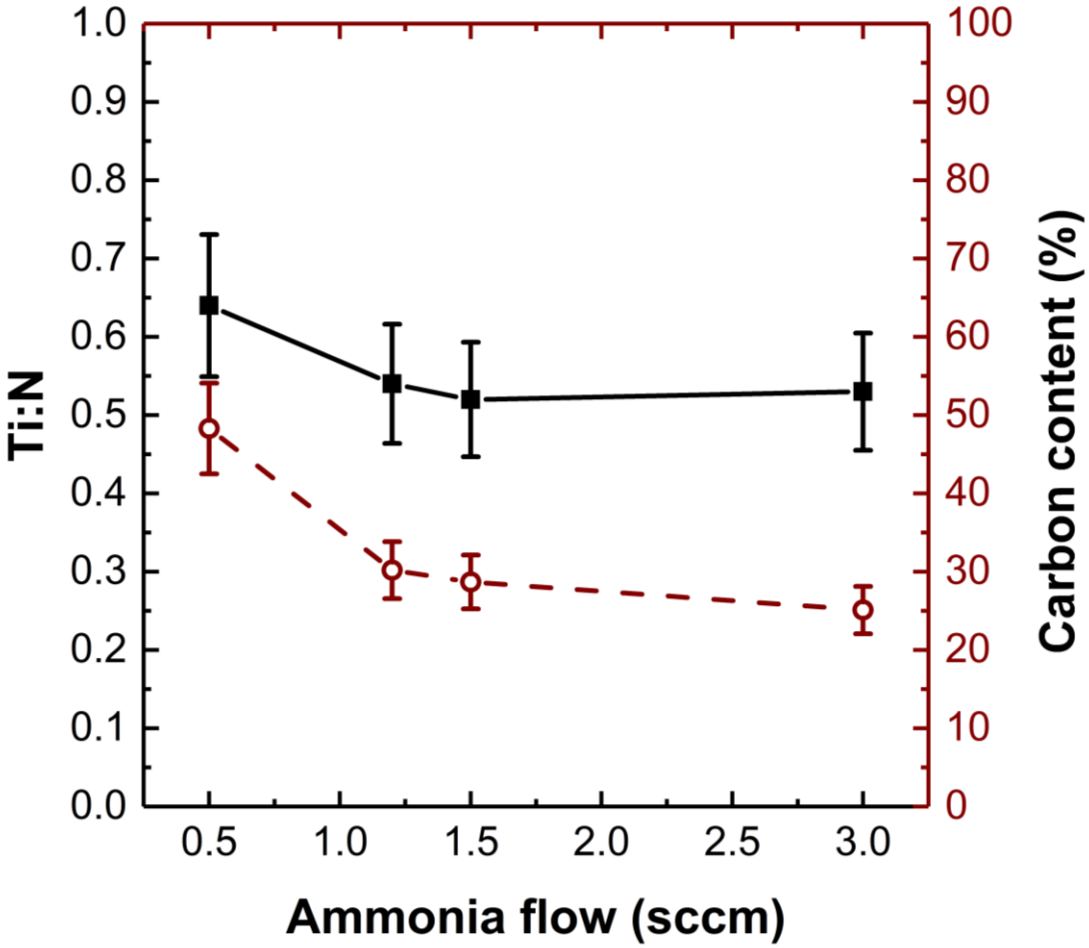

Figure 7.2.4: Titanium to nitrogen ration and carbon content of TiN NCs with respect to ammonia flow.

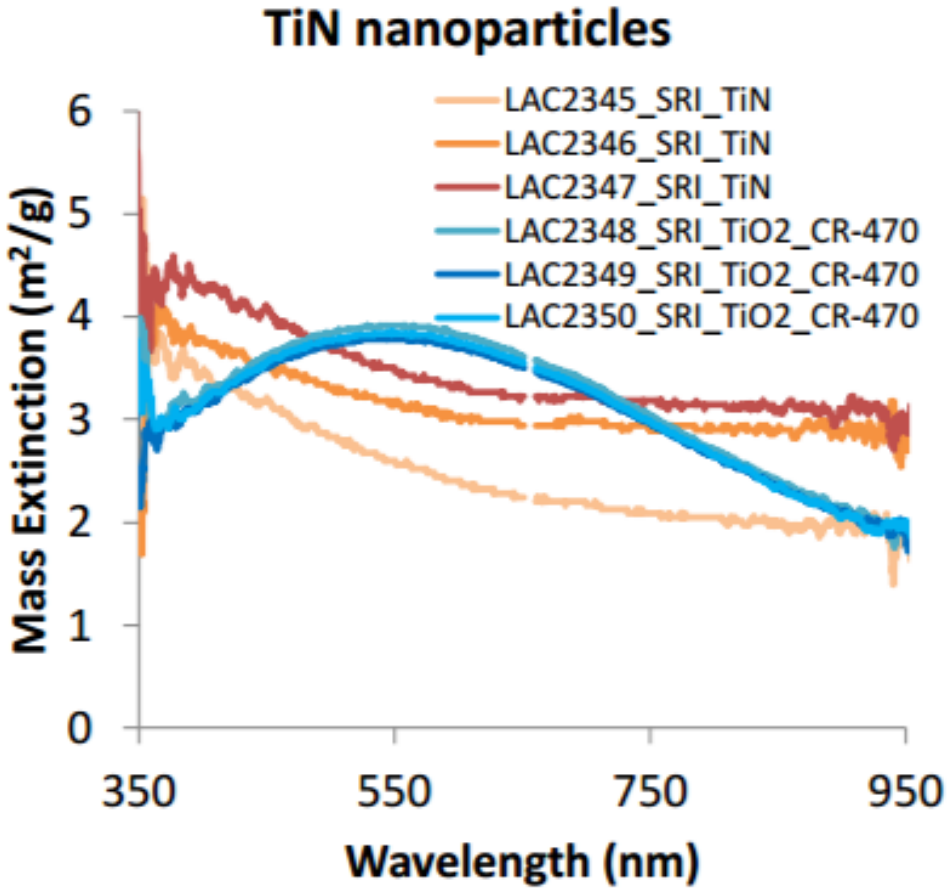

Figure 7.2.5: Obscurant data of TiN NCs provided by NanoComposix. TiN performs similarly to the current industry standard for obscurant materials, TiO2.